

# Controlling interfacial reduction kinetics and suppressing electrochemical oscillations in $\text{Li}_4\text{Ti}_5\text{O}_{12}$ thin-film anodes

*Yue Chen,<sup>1,2,⊥</sup> Handian Pan,<sup>1,3,⊥</sup> Chun Lin,<sup>1,3</sup> Jiaxin Li,<sup>1,3\*</sup> Rongsheng Cai,<sup>4</sup> Sarah J. Haigh,<sup>4</sup> Guiying Zhao,<sup>1,5</sup> Jianmin Zhang,<sup>1\*</sup> Yingbin Lin,<sup>1,5</sup> Oleg V. Kolosov,<sup>2\*</sup> and Zhigao Huang<sup>1,5\*</sup>*

<sup>1</sup>College of Physics and Energy, Fujian Normal University, Fujian Provincial Key Laboratory of Quantum Manipulation and New Energy Materials, Fuzhou, 350117, China

<sup>2</sup>Physics Department, Lancaster University, LA1 4YB, UK

<sup>3</sup>Fujian Provincial Engineering Technical Research Centre of Solar-Energy Conversion and Stored Energy, Fuzhou, 350117, China

<sup>4</sup>Department of Materials, University of Manchester, Manchester, M13 9PL, UK

<sup>5</sup>Fujian Provincial Collaborative Innovation Center for Advanced High-Field Superconducting Materials and Engineering, Fuzhou, 350117, China

## Abstract

Understanding the fundamentals of surface decoration effects in phase-separation materials, such as lithium titanate (LTO), is important for optimizing the lithium-ion battery (LIB) performance. LTO polycrystalline thin-film electrodes with and without doped Al-ZnO(AZO) surface coating decoration are used as ideal models to gain insights into the mechanisms involved. Operando shear force modulation spectroscopy was used to observe for the first time the three-dimensional nanoscale dynamics of solid-electrolyte-interphase(SEI) formation on the electrode surfaces, confirming that the AZO coating is electrochemically converted into a stiff, homogenous SEI layer that protects the surface from the electrolyte-induced decomposition. This AZO layer and its resultant artificial SEI-layer have higher Li-ion transport rates than the unmodified surface. These layers can reduce barriers to surface nucleation and facilitate rapid-redistribution of lithium-ions during the  $\text{Li}_4\text{Ti}_5\text{O}_{12} \rightleftharpoons \text{Li}_7\text{Ti}_5\text{O}_{12}$  phase separation, significantly inhibiting the orderly collective phase-separation behavior (electrochemical oscillation) in the LTO electrode. The suppressed voltage oscillations indicates more homogeneous local exchange current density and de-/intercalation states with the decorated electrodes, thereby extending their battery efficiency and long-term cycling stability. This work highlights the ultimate importance of surface treatment for LIB materials for determining their phase transition during the intercalation/deintercalation and provides a clear pathway to improving the LIB performance by nanoscale surface engineering.

## Keywords:

Lithium titanate thin film electrode; Lithium battery performance; Operando shear force spectroscopy; Electrochemical oscillation behavior; surface decoration engineering.

## 1. Introduction

Interface modification has been demonstrated as the most effective strategy to improve electrode-electrolyte interfacial properties and compatibility,<sup>[1,2]</sup> by stabilizing the crystalline surface structure of the electrodes,<sup>[3]</sup> accelerating lithium-ions transportation through the electrode-electrolyte interfaces (EEI),<sup>[4]</sup> and slowing solid-electrolyte-interphase (SEI) formation. Nonetheless, there has been no detailed investigation of the effects of surface-coatings on the phase-separation behavior in Lithium Titanium Oxide (LTO) anode, which suffer from sluggish two-phase transition kinetics during lithiation/delithiation.<sup>[5,6]</sup>

Zhou's group reported for the first time statistically significant oscillations in the galvanostatic voltage curves (electrochemical oscillation) for surface-treated LTO anodes.<sup>[7]</sup> Interestingly, their experiment demonstrated that the electrochemical oscillation of the surface-treated LTO anode is due to the 'collective electrochemical intercalation/deintercalation' within several-million active electrode particles participating in  $\text{Li}_7\text{Ti}_5\text{O}_{12} \rightleftharpoons \text{Li}_4\text{Ti}_5\text{O}_{12}$  phase separation. The authors attributed this electrochemical oscillation to the specific surface treatment and showed that carbon additions are necessary to observe this effect. However, the effects of carbon surface treatment, as well as the resultant high levels of rutile-TiO<sub>2</sub> as a phase impurity (19.55 wt%), were not explicitly discussed in this

report.<sup>[7]</sup> More recently, the positive effect of a surface carbon coating layer on the phase transition kinetics of a similar two-phase transition battery material, lithium iron phosphate (LFP), have been reported.<sup>[8]</sup> It was suggested that enhanced surface diffusion of lithium could play a key role in tuning the phase transformation in LFP electrodes.<sup>[9-11]</sup> These studies highlight that the importance of surface treatment for determining the electrochemical performance of phase-separation electrode materials like LFP/LTO cannot be overestimated, and a deeper investigation of underlying mechanisms could rapidly accelerate battery development.

Setting up the appropriate validated model system is essential to reveal mechanistic insights in a multi-particle phase-separation system with mosaic instability.<sup>[12]</sup> Composite electrodes contains binders, conductive agents, as well as associated grain boundaries and interfaces. These will introduce additional complexity to the electrochemical oscillation behavior of the composite electrodes and could inhibit effective interpretation of the bulk effects of surface treatments. For our experimental model, we therefore chose to prepare binder and conductive additive-free LTO thin-film electrodes, as well as to introduce AZO surface coatings to manipulate LTO electrode-electrolyte interfacial properties. It is also worth noting that, although a wide range of materials, including carbon,<sup>[13]</sup> Al<sub>2</sub>O<sub>3</sub>,<sup>[14]</sup> V<sub>2</sub>O<sub>3</sub>,<sup>[15]</sup> and ZnO/AZO,<sup>[16,17]</sup> have been tested as coating/decoration materials with the aim of improving deep-delithiated LTO (discharge cut-off voltage < 1.0 V vs Li<sup>+</sup>/Li) electrochemical performance, intensive debate remains regarding whether the coating layers retain the original chemistry or convert into a reduction protection layer with distinct physico-chemical properties. In other words, apart from the bulk effect of phase-separation, the mechanism of how a thin coating layer on the LTO anode can increase the EEI interfacial stability and lithium transportation kinetics is not yet understood.

*Operando* characterization techniques with high-spatial/temporal resolution can overcome the limitations of static and destructive characterization methods, making them key to studying the nanoscale physical-chemical processes occurring in battery materials.<sup>[18]</sup> Using our LTO thin-film electrode as a model sample that effectively represents the electrode-coating layer-electrolyte multi-interface structure, in this work, we study the dynamic SEI formation processes in LTO electrodes with and without AZO coating by *operando* shear force modulation microscopy (SFMM) in a liquid electrolyte environment (see supporting information (SI) Figure S1 for detailed methods). We found the coating layer transformed to an AZO-generated SEI layer consisting of compact Li-Zn alloy and Li<sub>2</sub>O domains, which form a highly efficient ion-conducting matrix, while protecting the electrode surface from being decomposed by the electrolyte, thereby drastically improving the batteries cycling stability and rate performance. Benefiting from the high lithium-ion diffusion rate within this artificial AZO induced SEI layer, the reduced nucleation barrier then inhibits intrinsic electrochemical oscillation in the LTO thin-film electrode, resulting in the disappearance of voltage oscillation in the galvanostatic curves. Our results demonstrate that proper surface modification can not only modulate the surface conductivity and reductive capability, but also provide a major improvement of Li<sub>7</sub>Ti<sub>5</sub>O<sub>12</sub> ⇌ Li<sub>4</sub>Ti<sub>5</sub>O<sub>12</sub> phase transition kinetics for the electrode.

## 2. Results and discussion

### 2.1. Electrode structure characterization

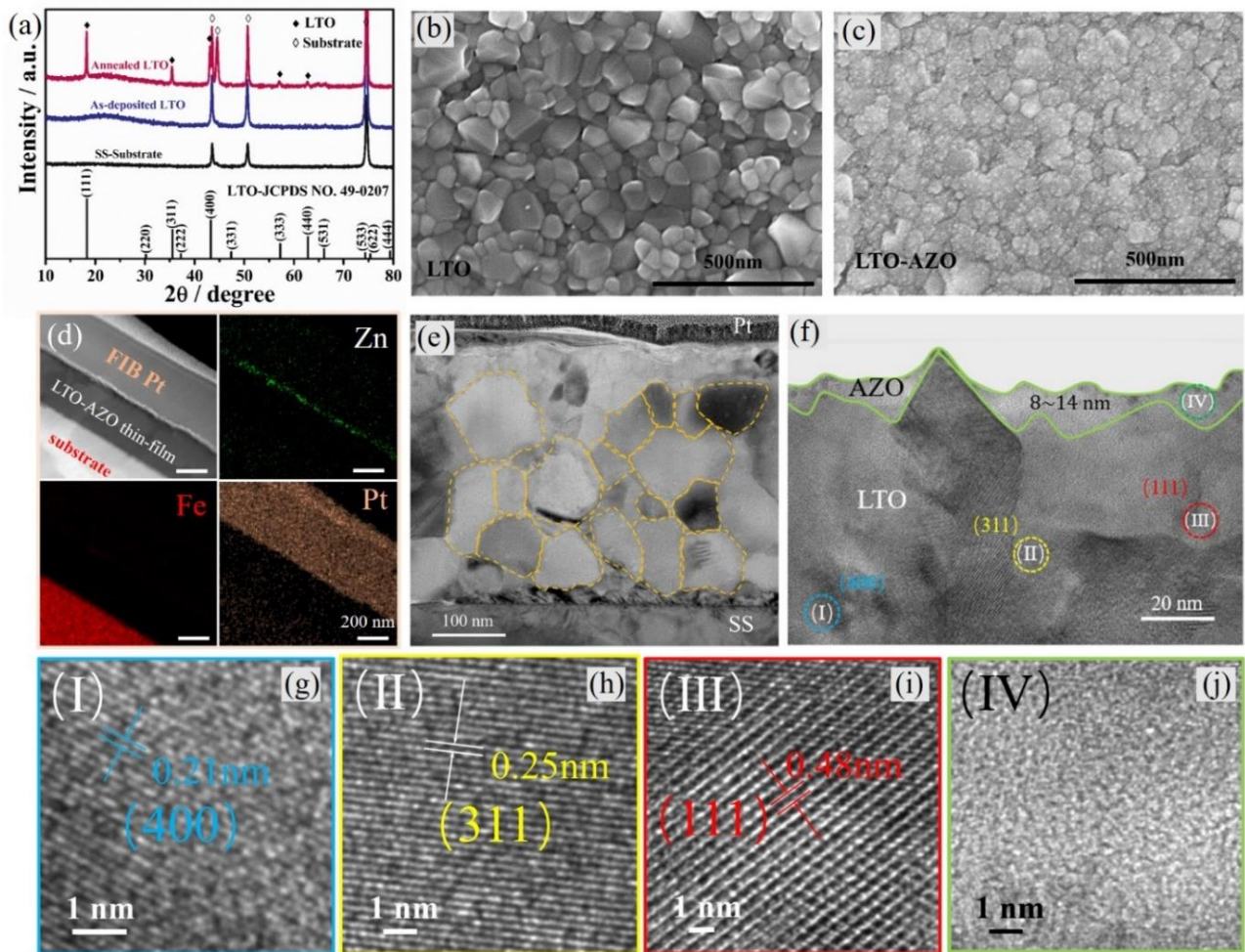


Figure 1. (a) XRD patterns from the stainless steel (SS) substrate, the as-deposited bare LTO film and the annealed LTO film; (b) secondary electron SEM images of the bare LTO film and (c) AZO(60)-LTO film (representative SEM images for AZO(30)-LTO and AZO(90)-LTO samples can be found in SI section 5); (d-j) Cross-sectional (S)TEM investigation of the AZO(60)-LTO film: (d) HAADF-STEM image of AZO-LTO cut by FIB; (e) HR-TEM image of the AZO(60)-LTO film with higher magnification view for the four dashed areas labelled I-IV indicated in (g-j), the Pt protective layer nano-structure and Zn element line scan was displayed in the SI section 5, Figure S5 a-b.

First, the bare LTO electrode material was prepared as well as similar samples where AZO was sputtered on the surface for 30, 60 and 90 seconds (referred to as AZO(30)-LTO, AZO(60)-LTO and AZO(90)-LTO films respectively). XRD patterns of the as-deposited and annealed bare LTO thin films are compared in Figure 1a. All the sharp diffraction peaks present for the as-deposited film are those of the stainless steel (SS) substrate, demonstrating that the as-deposited film is amorphous. After the annealing treatment, several additional diffraction peaks appear in the pattern, corresponding to the (111), (311) and (400) crystal planes of the cubic spinel LTO phase (JCPDS No. 49-0207). These diffraction data indicate the highly crystalline nature of the annealed LTO thin-film samples. The XRD patterns of the surface coated AZO(30)-LTO, AZO(60)-LTO and AZO(90)-LTO films can be found in Figure S2. Nevertheless, the existence of these thin AZO coating layers was confirmed by Raman spectroscopy and

conductive atomic force microscopy (C-AFM), as shown in SI Figure S3.

The microstructures of the LTO thin-film electrodes were further characterized using electron microscopy. Figures 1b and 1c show scanning electron microscopy (SEM) images of the surface of the annealed LTO film and of the 60 seconds AZO decorated LTO (AZO(60)-LTO), respectively. A surface grain size of  $\sim 70$  nm is observed for the bare LTO (the grain size distribution statistics can be found in Figure S4 a-b), and AZO(60)-LTO surface is covered by a coating layer with fine nanostructure after 60 seconds sputtering of AZO. The coating layer becomes more visible for longer sputtering times (Figure S6). Energy dispersive x-ray spectroscopy (EDS) measurements in the SEM reveal an even distribution of Zn and Al on the AZO(60)-LTO sample surface (Figure S7). To determine the thickness and crystal structures of the LTO and the AZO coating layer more precisely, high resolution EDS and (scanning) transmission electron microscopy ((S)TEM) measurements were carried out for thin-film cross-sections prepared by focused ion beam (FIB) milling. Figure 1c shows STEM-EDS elemental mapping of the AZO(60)-LTO film cross-section, where the thin Zn layer confirms the presence of AZO on the LTO surface (no Zn-layer signal can be observed in the bare LTO sample as shown in Figure S5). The Fe and Pt elemental signals come from the SS substrate and the protective Pt surface layer required for FIB sample preparation, respectively. Figure 1e shows the cross-sectional HR-TEM image of the AZO(60)-LTO film where a grain size of  $\sim 90$  nm is visible in the LTO. The statistical distribution of grain sizes obtained from the cross-section HR-TEM (Figure S4 c) shows a slightly higher bulk grain size value comparing to the surface grain size analyzed by SEM. This may be due to interior grain growth during annealing of the LTO film. Figure 1f shows an enlarged view of the LTO-AZO interface, where the  $\sim 10$  nm thick amorphous AZO layer is visible atop of a polycrystalline LTO film. The AZO layer can be distinguished from the Pt protective coating from the present of Zn in the ESD elemental map (Figure S5). Analysis of the interplanar spacings of each region in the LTO confirms the cubic spinal LTO phase (spacings of 0.48 nm, 0.25 nm and 0.21 nm, correspond to the (111), (311) and (400) crystal planes, respectively). The selected area electron diffraction (SAED) patterns acquired from the LTO layer (Figure S8) revealed crystalline diffraction rings which could be indexed to the expected LTO crystal planes. The absence of visible crystal structure in the AZO layer suggests this is amorphous. Overall, the structural characterization confirms the model structure of a polycrystalline LTO thin-film electrode, with an ultra-thin amorphous AZO coating layer.

## 2.2. Electrochemical performance

The electrochemical performance of the bare LTO and various AZO-LTO thin-film electrodes were evaluated using coin half cells. The details of thin-film areal capacity evaluations and calculations can be found in the supporting information section 6. Figures 2a and 2b show the cycling and rate performances of the bare LTO and AZO-LTO film electrodes at room temperature. From the figures, it can be found that the proper AZO surface modification has significant influence on the electrode's electrochemical performance. Especially, AZO(60)-LTO displays the best cycling performance. The pure LTO thin-film electrode has an initial capacity of  $27.4 \mu\text{Ah cm}^{-2}$ , while its reversible capacity gradually decreases to  $\sim 17.8 \mu\text{Ah cm}^{-2}$  over the first 100 cycles and then remains

approximately stable. For AZO(30)-LTO, the cycling performance is similar to bare LTO, apart from a slightly higher initial capacity ( $30.6 \mu\text{Ah cm}^{-2}$ ) demonstrating that only 30 seconds of AZO sputtering does not make much of a difference to the LTO cycling performance. The decorated AZO coating on the AZO(30)-LTO electrode appears to form ‘nano-islands’, aggregating in the ‘valleys’ between LTO grains, rather than a uniform decoration layer (Figure S6). In this case, the AZO coating layer after reduction decomposition cannot form the continuous protective layer needed to effectively suppress the electrolyte decomposition, as well as to provide low charge transfer resistance. Therefore, the cycling performance and rate capability of AZO(30)-LTO is similar to the bare LTO. The AZO(90)-LTO film had an even higher initial capacity of over  $33.4 \mu\text{Ah cm}^{-2}$ , and then gradually decayed to  $\sim 16.7 \mu\text{Ah cm}^{-2}$  after 300 cycles. This high initial capacity derives from the electrochemically active AZO coating layer and the irreversible SEI formation,<sup>[19]</sup> as well as the surface lithium storage<sup>[20]</sup> that contributes to the extra initial Faraday capacity. However, a thicker AZO coating layer may not be able to be fully and uniformly reduced into the highly conductive Li-Zn/Li<sub>2</sub>O/AlF<sub>3</sub> protection layer. Therefore, the charge transfer and ion diffusion through this inhomogeneous solid-liquid interface was reduced, resulting in a high charge transfer resistance. Moreover, upon cycling, inhomogeneous lithiation/de-lithiation states present on the AZO(90)-LTO film surface can generate local strain especially in low voltage range, potentially causing damage to the local crystal structure and surface relaxation,<sup>[21]</sup> with all these being detrimental to the electrode performance of AZO(90)-LTO. The AZO(60)-LTO shows the best cycling stability and is still able to deliver  $\sim 22.3 \mu\text{Ah cm}^{-2}$  after 300 cycles. The initial capacities of all AZO decorated LTO are higher than the bare LTO, indicating that the AZO coating partially contributes to the magnitude of the irreversible capacity during the first cycle.<sup>[22]</sup> Cyclic voltammetry measurements also confirm that a protective layer was formed on the electrode surface via the electrochemical decomposition of AZO, the so called ‘self-sacrificing effect’ (see Figure S9). Figure 2b shows the rate performances of the four samples at various charge/discharge rates (0.2 C, 1 C, 2 C, 5 C and 10 C). At 1 C cycle rate, we find that the average capacity of the bare LTO film is  $\sim 24.8 \mu\text{Ah cm}^{-2}$ , and the average capacities of AZO(30)-LTO and AZO(90)-LTO films are slightly less than  $22.3 \mu\text{Ah cm}^{-2}$ ; while the average capacity of the AZO(60)-LTO film can reach as high as  $28.2 \mu\text{Ah cm}^{-2}$ . Moreover, as the rate increases, the observed capacity of AZO(30)-LTO and AZO(90)-LTO become lower than bare LTO, while the capacity of AZO(60)-LTO stays higher than bare LTO. The reduced rate performance of AZO(30)-LTO and AZO(90)-LTO is directly linked to their high charge transfer resistance at the electrode-electrolyte interfaces.

The electrochemical performances of the bare LTO and AZO decorated LTO was also studied in a high-temperature environment, in which lithium diffusion is activated and more serious electrolyte decompositions is commonly observed.<sup>[19]</sup> Figures 2c and 2d show their cycling and rate performances between 0.1 V and 3.0 V at 60 °C. The AZO(60)-LTO film shows good cycle stability at high temperature and high rate (5 C). The specific capacity remains at  $22.3 \mu\text{Ah cm}^{-2}$  even after 500 cycles. By contrast, after 500 cycles, the bare LTO film delivers a specific capacity of just  $13.4 \mu\text{Ah cm}^{-2}$ . This high-temperature cycling performance degradation seen for these LTO films is similar to that observed previously for LTO composite electrodes due to electrolyte decomposition.<sup>[19]</sup> As shown in Figure 2d, comparing AZO(90)-LTO with the bare LTO samples reveals that their capacities are similar at low rates,

but at high rates, AZO(90)-LTO delivers higher capacity. This indicates that uniform coating of the LTO surface with too thick an AZO layer may still resist the electrolyte decomposition at elevated temperature. However, AZO(60)-LTO displays the best rate performance at all charge/discharge rates, delivering capacities of  $\sim 26.1 \mu\text{Ah cm}^{-2}$  and  $\sim 24.1 \mu\text{Ah cm}^{-2}$  at 5 C and 10 C, respectively. Therefore, these results indicate that an AZO coating layer of appropriate thickness can improve the charge transfer and lithium diffusion, which results in better rate performances when cycling between 0.1-3.0 V both at room temperature and at elevated temperature. This could be attributed to the protection from an AZO-derived SEI layer which prevents serious electrolyte decomposition on the electrode surface at elevated temperature.

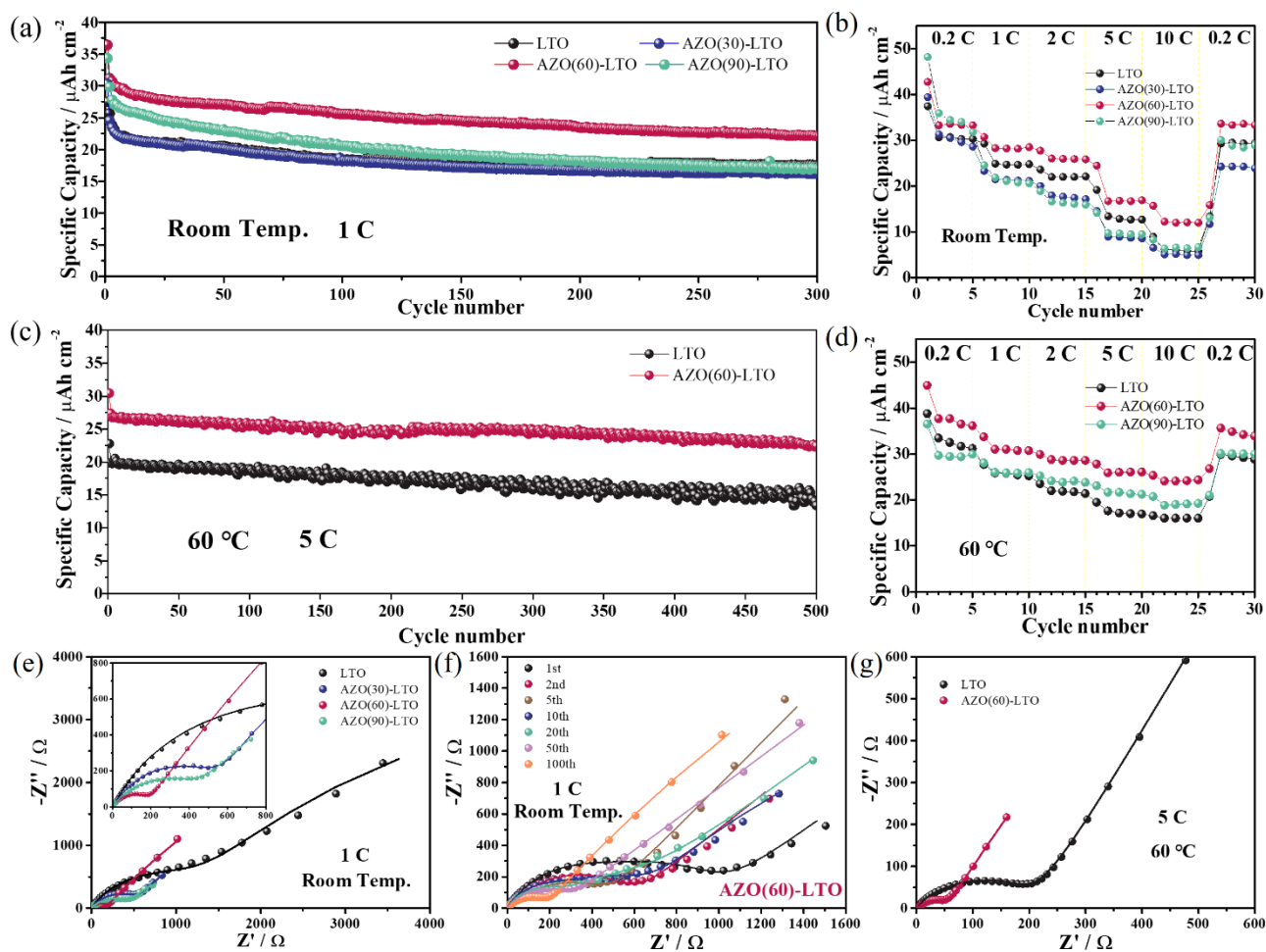


Figure 2 Cycling and rate performance of bare LTO, AZO(30)-LTO, AZO(60)-LTO and AZO(90)-LTO between 0.1 V and 3.0 V. (a) cycling performance at room temperature; (b) rate performance at room temperature; (c) cycling performance at 60 °C; (d) rate performance at 60 °C; (e) Nyquist plots of LTO and AZO-LTO thin-film electrodes after 100 cycles at 1 C and room temperature; (f) Nyquist plots of AZO(60)-LTO film electrode after different charge/discharge cycles and (g) LTO film and AZO(60)-LTO film electrodes after 100 cycles at 5 C and 60 °C.

Electrochemical impedance spectroscopy (EIS) measurements were next employed to understand the origin of the rate performance differences. The equivalent circuit model and lithium diffusion calculation details can be found

in the SI Figures S10 and S11. Figures. 2e and 2f show the EIS of coin cells that contained bare LTO or AZO-LTO electrodes. All curves contain a semicircle reflecting the charge transfer process in the high-frequency region and a slant line corresponding to the lithium-ion diffusion process in the low-frequency region.<sup>[23]</sup> The electrolyte Ohmic resistance ( $R_e$ ) relates to the intercept of the high-frequency region, and diameter of the semicircle is proportional to charge transfer resistance ( $R_{ct}$ ).<sup>[24]</sup> It can be seen from Figure 2e that, after 100 cycles at room temperature, the  $R_{ct}$  values of all AZO-LTO samples were significantly lower than that of the bare LTO. Amongst them, the  $R_{ct}$  of the AZO(60)-LTO cell is the smallest ( $\sim 160 \Omega$ ), which indicates that the AZO coating suppresses the increase of impedance during cycling. In order to further understand the mechanism of this suppressed impedance increase, we carried out EIS tests in AZO(60)-LTO cells after different numbers of cycles. As shown in Figure 2f, with increasing cycle number, the charge transfer resistance of the electrode decreased continuously. This could be because of the gradual reduction and conversion of the initial AZO coating layer into an SEI layer with high ionic conductivity. EIS testing after cycling at 5 C and 60 °C also showed similar results. As shown in Figure 2g, the  $R_{ct}$  of the AZO(60)-LTO electrode was only about 50  $\Omega$ , and the bare LTO electrode was more than four times higher than that value. The lower charge transfer resistance of AZO(60)-LTO at elevated temperature could be the reason for its better rate performance compared to bare LTO, as shown in Figure 2b. The EIS results show that the AZO coating reduces the charge transfer resistance of the cells, which is beneficial for the kinetics of electron and lithium-ion transportation within the cell, and therefore will result in a better cycle and rate performance. Based on the EIS data in Figure 2e, the chemical diffusion coefficient of  $\text{Li}^+$  ( $D_{\text{Li}^+}$ ) was calculated (see SI section 6 for details). After 100 cycles at room temperature and 1 C, the  $D_{\text{Li}^+}$  of bare LTO, AZO(30)-LTO, AZO(60)-LTO and AZO(90)-LTO electrodes are around  $3.30 \times 10^{-12} \text{ cm}^2\text{s}^{-1}$ ,  $6.81 \times 10^{-12} \text{ cm}^2\text{s}^{-1}$ ,  $3.12 \times 10^{-11} \text{ cm}^2\text{s}^{-1}$  and  $9.12 \times 10^{-12} \text{ cm}^2\text{s}^{-1}$ , respectively. In other words, the proper AZO coating layer can improve lithium-ion transportation, with the diffusivity being highest in AZO(60)-LTO, which showed a value nearly an order of magnitude higher than bare LTO.

### 2.3. SEI formation and compositional analysis

EIS measurements show that the AZO(60)-LTO cell has initially high impedance before cycling, while the  $R_{ct}$  values dramatically decrease during the initial cycles (Figure 2f). The boosted charge transfer properties should relate to partial reduction of the AZO coating layers and consequential SEI formation. Real-space observation of the SEI formation in the liquid environment on both electrodes surface can provide direct evidence for this hypothesis. *Operando* AFM has demonstrated its versatility for the real-space observation of SEI formation in battery materials,<sup>[25]</sup> however, few reports have applied shear vibration interactions between the tip-sample, which is extremely sensitive to the viscoelastic SEI layer, to monitor the dynamic growth of SEI layers. We therefore first applied the *operando* shear force modulation microscopy (SFMM) technique here to monitor the initial dynamic SEI formation process on bare LTO and on the AZO(60)-LTO electrode surface. A detailed instrument sketch and explanation of the measurement principles is provided in the SI section 1.

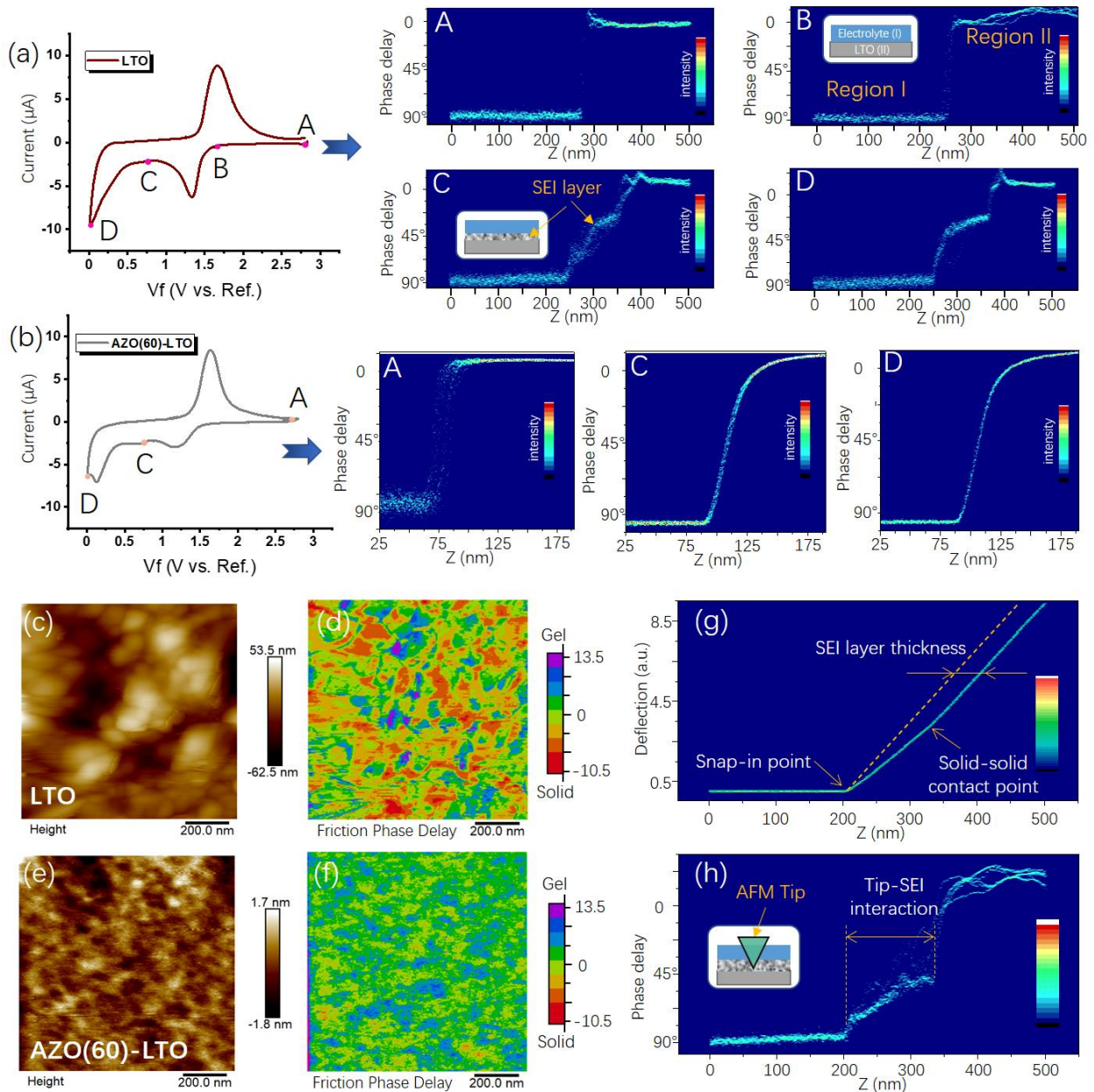


Figure 3. 2-D *operando* shear force AFM spectra of (a) bare LTO and (b) AZO(60)-LTO thin-film electrodes at different cathodic voltages during the first CV cathodic scan (scan rate 0.5 mv/s, active material mass may vary due to the *operando* cell structure, measurement sample points: A=2.8 V, B=1.7 V, C=0.75 V and D=0.1 V). The topography (c) and torsional phase (d) images of bare LTO after the first cathodic scan. The topography (e) and torsional phase (f) images of AZO(60)-LTO after the first cathodic scan. The vertical deflection (g) vs piezo Z movement and the corresponding phase delay (h) vs piezo Z movement.

Figure 3 shows the *operando* SFMM measurements obtained for the LTO and AZO(60)-LTO samples. The shear force approach-retract spectra were recorded at different voltages during the first CV cathodic scan. The Z piezo moved from 0 nm to the pre-set vertical deflection set-points, ramping the tip toward the sample surface. During ramping, the vertical displacement of the tip, as well as the lateral vibration phase were recorded simultaneously as reported elsewhere.<sup>[26, 27]</sup> As can be seen in the 2-D *operando* shear force spectra in Figure 3a, at open circuit potential

(spectrum A), the torsion phase spectrum suddenly jumps from 90 degree to 0 degree as long as the tip was contacting the electrode surface (at around  $Z=275$  nm), indicating a clean surface without SEI. This ‘jumping’ of the torsion phase can still be observed at a cathodic voltage around 1.6 V as shown in spectrum B, where region I and II correspond to the electrolyte and LTO electrode, respectively. However, as the cathodic voltage is scanned down to around 0.75 V, a transition region in the phase approaching curves corresponding to an approximately 90 degrees phase shift, emerges as shown in spectra C and D in Figure 3a. According to the phase delay analysis (Figure S1), this should be attributed to the formation of viscous SEI layers on the solid LTO surface. Interestingly, one can find in Figure 4b that this significant ‘jumping’ transition does not appear on the AZO(60)-LTO samples during the whole cathodic scan from open circuit potential (OCP) down to 0.1 V, indicating a dramatic difference of the tip-contact status compared to bare LTO. Immediately after the tip contacts the AZO(60)-LTO sample surface, the phase lag decreases with an increase of the vertical displacement ( $Z$ ), which similar trend was reported for solid-solid contact of the tip with silicon oxide.<sup>[28]</sup> In other words, the ‘missing’ gel-like transition region in the torsion phase approaching spectra in the AZO(60)-LTO surface indicates the absence of a loose/viscous SEI layer formed on the electrode surface, indicating that the AZO(60)-LTO surface SEI layer is a mechanically stronger and stiffer surface passivation layer.

The homogeneity of the SEI formed on LTO and AZO(60)-LTO was further characterized by SFMM mapping with Figures 3c-f showing both the topography and phase images recorded simultaneously. By comparing Figures 3c with 3e, one notices that the bare LTO surface shows a rough topography with many irregular SEI bumps, while the AZO(60)-LTO surface was covered by a smooth passivation layer with finer structure. Additionally, Figures 3d and 3f are the phase images, recording the same areas as in the topography images in Figures 3c and 3e, respectively. It is clear that LTO surface shows much more inhomogeneity in phase delay comparing to AZO(60)-LTO, which confirms that a more uniform SEI layer with more uniform chemical composition was obtained on the AZO modified LTO surface after the first cathodic scan, compared to the bare LTO. Figures 3g and 3h show the vertical deflection and the corresponding torsional phase approaching spectra at the central position of Figure 3d. Two distinct regions with different slopes, corresponding to the tip-SEI indentation ( $210 < Z < 340$  nm) and pure tip bending ( $Z > 340$  nm) regions, can be observed in the deflection approaching spectra. These two regions also show distinct phase response as shown in Figure 3h. Furthermore, by processing the vertical deflection curves assuming that the tip deflection is equal to the sample displacement in the region of the solid-solid tip-sample contact ( $Z > 340$  nm), the SEI thickness can be reliably determined by measuring the horizontal distance between the raw force-spectrum curves and the dashed line corresponding to the solid-solid contact, as shown in Figure 3g. The obtained SEI thickness is around  $45 \pm 5$  nm at the centre point in Figure 3c. *Operando* SFMM measurements in this report therefore allow direct visualization and quantification of the dynamic growth of SEI layers of the order of a few tens of nanometers thick, and to identify inhomogeneity in SEI chemical components that have different viscosities. The components and chemical bonds of these distinct SEI layers were further evaluated by *post-mortem* X-ray photoelectron spectroscopy (XPS) (see SI Figure S12). It is found that the SEI layers formed on the bare LTO surface contain high proportions

of organic species mixed with inorganic LiF/Li<sub>2</sub>CO<sub>3</sub>, while on the AZO(60)-LTO electrode surface, the AZO coating layers were converted into Li/Zn-F and Li<sub>2</sub>CO<sub>3</sub> rich inorganic reduction products, resisting the formation of inorganic decomposition products. This is consistent with *operando* SFMM characterization that show a mechanically much more homogenous SEI layer on the AZO-LTO than was formed on the bare LTO electrode surface.

#### 2.4. Suppressed interfacial reduction kinetics (surface effect)

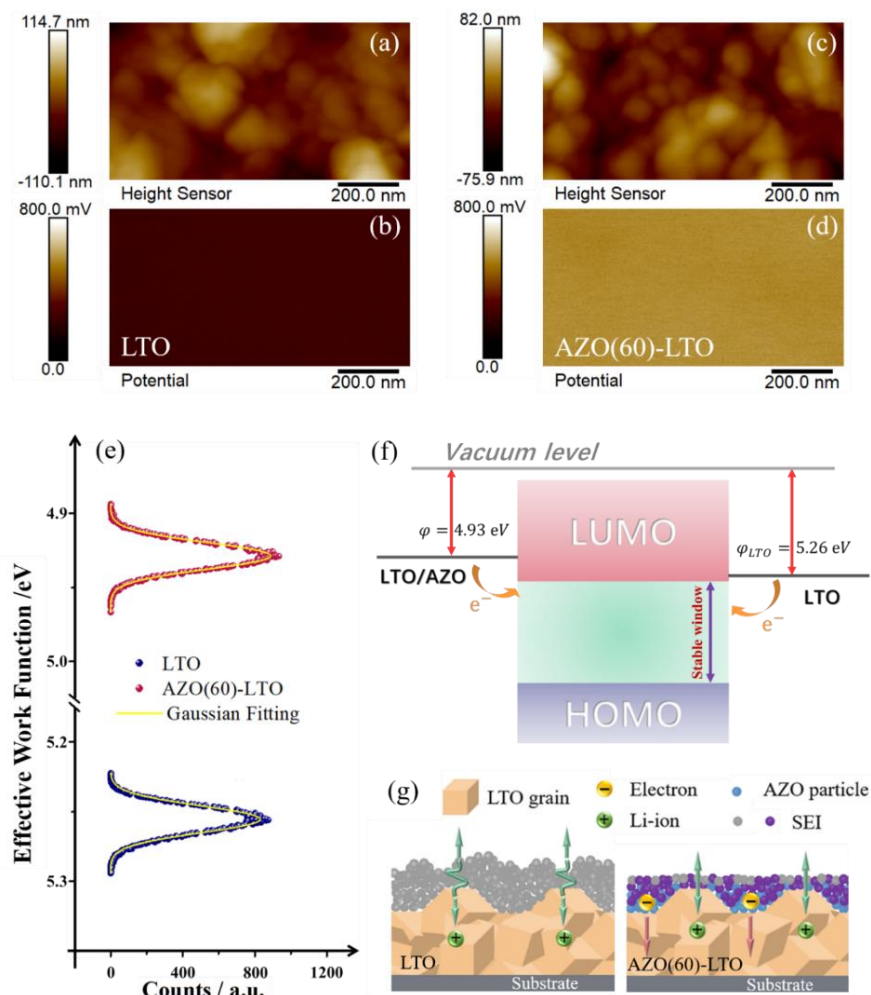


Figure 4. Surface morphologies (a) and potential maps (b) of bare LTO; Surface morphologies (c) and potential maps (d) of AZO(60)-LTO thin-film electrodes detected by KPFM; (e) Effective work functions LTO films and AZO(60)-LTO films; (f) Schematic energy diagrams of the electrode/electrolyte interfaces. (g) SEI formation model on both electrode surfaces.

Here we have demonstrated that the surface decoration of LTO electrodes with AZO metal oxide is an effective method for improving the electrode-electrolyte interface stability, which increases the batteries coulombic efficiency and rate performance. Nevertheless, in order to implement these, we need to further investigate the underlying physical and chemical phenomenon. Our EIS, SFMM and XPS characterization results above confirm that the AZO decoration layer can be electrochemically reduced to form an Li-Zn rich passivation layer which has high lithium-ion conductivity and mechanical stiffness, assisting the uniform intercalation of lithium ions and inhibiting SEI film

growth. Yet the question remains - how can this AZO coating layer spontaneously exhibit “self-sacrificing” behaviour while also preventing further electrolyte decomposition?

The formation of the SEI at the anode-electrolyte interface is thermodynamically governed by the alignment of the reduction energy level ( $-eE_{\text{reduction}}$ ) of the electrolyte molecules and the Fermi level of the anode surface.<sup>[29]</sup> The surface electronic structure of the anodic electrode, which determines the reduction kinetics of the electrolyte relative to the anode surface, has been proven to be a critical parameter determining SEI formation and composition.<sup>[30]</sup> Therefore, Kelvin probe force microscopy (KPFM) measurements were carried out to understand how the electrode material itself affects the EEI interfacial stability and formation of the SEI. Figures. 4a-d show the surface potential and nanomorphology of the AZO coated LTO and bare LTO films measured by KPFM. From these, it is found that the surface potential of the thin-film electrode (AZO(60)-LTO) was dramatically increased by the AZO coating compared to bare LTO. The effective work functions (EWF) of each thin film electrode were further calculated from these surface potential maps, and the distribution functions are presented in Figure 4e. It is shown that the EWF of the AZO(60)-LTO electrode ( $\sim 4.93$  eV) is about 330 meV smaller than that of the bare LTO electrode ( $\sim 5.26$  eV). According to the energy level diagram in Figure 4f, one can conclude that, compared to the bare LTO electrode surface, AZO(60)-LTO with a smaller EWF value has higher reduction kinetics on the anode-electrolyte interface, which could facilitate the reduction reactions occurring on the electrode surface<sup>[30]</sup> even before the electrochemical cycling begins. Therefore, during the initial discharge process, the anion and solvent adsorption species inside the inner Helmholtz layer<sup>[31]</sup> tend to react with the AZO coating layer rather than the LTO; while, at low lithiation voltage, AZO was further reduced creating an ionically conductive passivation layer consisting of Li-Zn nanoparticles embedded in the  $\text{Li}_2\text{O}$  matrix, and therefore dramatically improving the cycle and rate performances of the LTO anode. This provides a clear explanation for the improved electrochemical performances observed in Figure 2, as well as the observed Li-Zn peaks in the XPS measurements (Figure S12). The self-sacrificial behavior of the surface coating layer in anode materials is not unexpected<sup>[32,33]</sup> as the working potential window is relatively low when compared to the coating layers on the battery cathode side. It is well accepted that the oxide decoration layers on cathode materials are relatively stable and act as a physical barrier blocking the corrosion effects of HF in the electrolyte,<sup>[34]</sup> with the boosted charge transport processes in these coating layers being attributable to the built-in electric field derived from the coating layer-cathode heterojunction.<sup>[35]</sup> Interestingly, our experiments with AZO coated LTO anodes suggested that the ‘local built-in electric field’ model<sup>[36, 37]</sup> might be not suitable for metal oxide decorated anode materials because the decoration layer can be reduced electrochemically during cycling. It is also worth mentioning that some oxygen vacancies, which could improve ionic/electronic transport and ion insertion/extraction on the electrode-electrolyte interface,<sup>[38]</sup> might be generated on the LTO surface by the AZO coating. This could also contribute to the enhanced charge transfer capability of the AZO coated electrode.

## 2.5 Inhibited electrochemical oscillation (bulk effect)

Here we explore the effects of the stabilized electrode-electrolyte interfacial structure on the phase-separation

kinetics of the LTO electrodes. In a recent report on electrochemical oscillation of LTO, the observed voltage oscillation during galvanostatic charge/discharge has been attributed to a ‘group-by-group’ phase transition path.<sup>[7,39]</sup> Since the ‘group-by-group’ phase transition path represents the electrode-scale bulk inhomogeneities in lithiation/delithiation that are closely associated with the amplified local exchange current density, the presence of oscillations may indicate accelerated electrode performance degradation.<sup>[40]</sup> We therefore carefully examine the voltage oscillations in our LTO thin film electrode model to better understand the effects of AZO surface treatment.

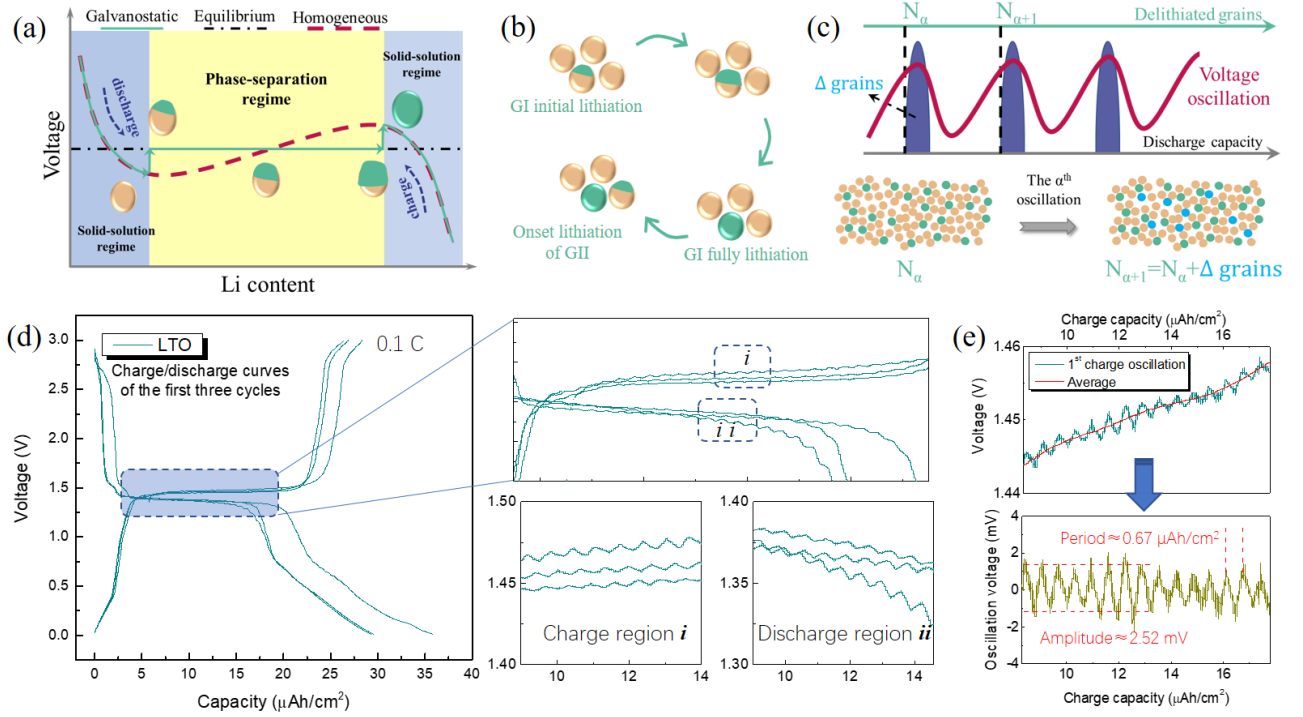


Figure 5 (a) The proposed open circuit voltage profiles of galvanostatic discharge and homogeneous lithiation in a single-grain. The galvanostatic process is the green solid line and the hypothesized homogeneous lithiation/delithiation process is represented by the red dashed line, and the two-phase equilibrant voltage is the black dashed horizontal centre line. (b) The voltage bump mechanism in a system with multiple particles due to the ‘‘mosaic instability’’, the onset lithiation of grain II (GII) happens only when grain I (GI) is fully lithiated; (c) The phase-separation occurs with certain active percentages of grains in the ‘‘Group-by-group model’’ ( $\Delta$ grains is the number of active grains/particles in each oscillation); (d) Electrochemical oscillation phenomenon seen in the galvanostatic charge/discharge curves of LTO samples at 0.1 C and (e) oscillation period and amplitude analysis.

To discuss the electrochemical oscillations of LTO electrodes, it is instructive to first look at the lithiation/delithiation induced voltage response of a single-grain with a non-monotonic chemical potential.<sup>[41,42]</sup> According to the regular solution model, the free energy of a homogenous phase transition for a single-grain can be described as:<sup>[41,42]</sup>

$$F(c, T) = \Omega c(1 - c) + k_B T [c \ln c + (1 - c) \ln(1 - c)] \quad (1)$$

Where  $c$  is the lithium concentration in the LTO single-grain,  $k_B$  is Boltzmann constant,  $T$  is absolute temperature, and  $\Omega$  is the constant representing the nearest-neighbor interaction between lithium ions within the host lattice. The

chemical potential  $\mu(c)$  can be obtained by differentiating the free energy with respect to lithium concentration:

$$\mu(c) = \Omega(1 - 2c) + k_B T \ln\left(\frac{c}{1-c}\right) \quad (2)$$

Therefore, the open circuit voltage  $V_{OCP}$  can be written as:

$$V_{OCP} = V_{EQ} - \frac{\mu(c)}{e} \quad (3)$$

Where  $V_{EQ}$  is equilibrium voltage, and  $e$  is electron charge. In figure 5a the red-dashed line shows the simulated open circuit voltage profiles based on equation (3). It is clearly that when entering the two-phase region, the filling/extraction of lithium-ions in a LTO single-grain will result in the observed “bump” in the galvanostatic voltage curve (green solid line) overshooting the two-phase equilibrium voltage (black dashed horizontal line). This voltage bump is a fundamental feature of the electrochemical oscillation phenomenon. Thus, extending this voltage bump phenomenon to a scenario where there are many particles, as shown in Figure 5b, the phase separation will follow a one-by-one pathway due to the “mosaic instability”, and thereby the galvanostatic voltage profile may exhibit many sudden rises and drops due to the sequential mosaic instability events.<sup>[39,42]</sup> However, for commercial LTO/LFP composite electrodes (consisting of about  $\sim 10^{10}$ - $10^9$  grains), the localized mosaic instability events randomly occur over the whole electrode during the charge/discharge and this smooths out the voltage bumps. As a result, a flat voltage plateau is usually observed in the two-phase regime of these multi-particle phase-separation composite electrodes.

Therefore, it is important to note that the voltage oscillations emerge only when the mosaic instability events occur discretely separated in time and space upon galvanostatic charge/discharge. Specifically, as shown in Figure 5c, during discharge, the phase separation concurrently occurs at each “group” of active crystal-grains (such as the  $N_\alpha$  group or  $N_{\alpha+1}$  group) when the voltage oscillations reach each peak/valley. This “group-by-group” model is a more realistic scenario consistent with experimental observations.<sup>[43,44]</sup>

As shown in Figure 5d, in the LTO thin-film anode, voltage oscillation was observed in both galvanostatic charge/discharge platforms during the initial cycling, while this oscillation disappears outside of the charge/discharge platforms (Figure S13). The oscillation signals on the charge/discharge platforms show a slightly increased amplitude after the first cycle, but almost identical frequency (period). This voltage oscillation can be attributed to the discrete nature of multi-particle phase-separated reactions as discussed above. The fraction of actively phase-separating particles ( $\Delta$ grains) can be further estimated by analyzing the charge/discharge voltage oscillation curves. As shown in Figure 5e, by subtracting the average line of the first charge, the obtained flattened oscillation signal shows an amplitude of about 2.52 mV and a period about 0.67  $\mu\text{Ah cm}^{-2}$ . Therefore, the estimated fraction of actively phase-separation particles is about 2.3%. Assuming a uniform grain-size distribution within the thin-film electrode, the estimated number of crystal grains in a LTO thin-film electrode is around  $\sim 10^{10}$ . Since the oscillating period (in capacity) is proportional to the number of active grains, each ‘group’ includes about  $\sim 2.3 \times 10^8$  grains, indicating that the collective phase separation of numerous grains in the LTO thin-film electrode is highly ordered. However, as shown in Figures 6a-c, the oscillation behaviour sensitively depends on the surface coating layer and

intercalation/deintercalation rate.

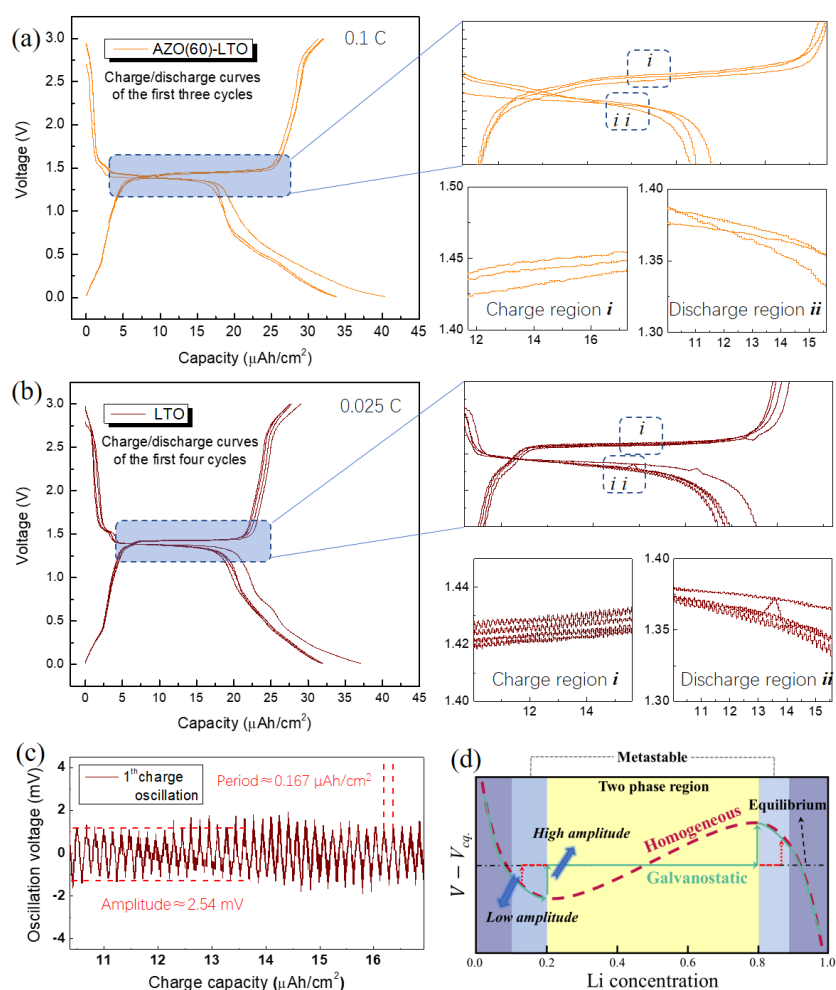


Figure 6 (a) Galvanostatic charge/discharge curves of AZO coated LTO samples at 0.1 C. (b) Electrochemical oscillation phenomenon in bare LTO sample at low charge/discharge current density (0.025 C) and (c) oscillation period and amplitude analysis. (d) Relation between lithium diffusion (redistribution capability) and electrochemical oscillation amplitudes.

As shown in Figure 6a, during the initial cycles, the AZO(60)-LTO does not show visible oscillation signals with a similar amplitude as LTO. As discussed in the *operando* SFMM and post-mortem XPS characterization sections, the self-sacrificing AZO coating produced a robust SEI layer with high conductivity which could accelerate the ion transportation and charge transfer on the EEI. This may be the reason why voltage oscillations cannot be observed in the AZO(60)-LTO electrode. The high electronic conductivity of the AZO coating layer and ionically conductive SEI layer benefits charge transportation and  $\text{Li}^+$  accumulation and the consequent lithium surface nucleation, which will trigger phase separation to enter the “metastable region” ahead of the unstable phase-separation regime as shown in Figure 6d.<sup>[7,11]</sup> As a result, not only the voltage bump was restrained in each single-grain (oscillation amplitude reducing), but the localized mosaic instability was also smoothed (periodicity destroyed or largely extended) over the whole thin-film electrode. By contrast, the LTO electrode forms a thick surface passivation layer, which reduces the lithium ‘wetting effect’ on the grain surface and therefore postpones the electrode

entering metastable phase-separation region, resulting in a “higher oscillation amplitude” fluctuation in the galvanostatic voltage curves as soon as it reaches the inflection point. This is also the reason why voltage oscillations were observed in the surface treated LTO samples with high proportion of impurity in Ref. 7, but disappeared in the AZO surface coated LTO in this study. The better surface lithium wetting effect in impurity-free LTO (reported in Ref. 7) and the AZO decorated LTO thin-film electrode reported here can both facilitate nucleation events on the LTO particle surface, as well as the rapid redistribution of electrons/lithium ions between the nano-grains,<sup>[11]</sup> therefore inhibiting the electrochemical oscillations. It also worth noting that the voltage oscillation disappeared in the AZO(60)-LTO electrode even at the first lithiation voltage platform, where the AZO-derived SEI is not fully formed on the electrode surface. Whether the disappearance of the oscillations shown here is related to the enhanced lithium-ion de-solvation processes or pre-cycle surface passivation layer needs to be further studied.

Compared to the electrochemical oscillation in Ref. 7, the significant difference seen in this study is the ratio of the no-oscillation region versus oscillation region in charge/discharge voltage platforms. In our study, voltage oscillation was observed during the whole phase-separation region, while the oscillation only began at the later part of the two-phase region for the previous report.<sup>[7]</sup> Interestingly, a simple calculation shows that the estimated initial total grain numbers in each LTO electrodes are of the order of  $\sim 10^{10}$ , which is at the same order as the onset of oscillation for the electrode grains/particles in Ref. 7. We therefore believe that, in our LTO thin film electrode, the grain number is small enough for stochastic fluctuation of mosaic instability events to induce the oscillatory phenomenon even at the initial phase-separation region (the beginning of charge/discharge voltage platforms). This also explains the electrochemical oscillation caused by the less active grains at low charge/discharge rate as shown in Figures 6b and 6c. From Figure 6c, it can be found that the voltage oscillation frequency of the bare LTO electrode was increased at lower charge/discharge rates. The reduced active grain friction (fewer active grains) during the entire phase-transition is enough to deliver the required galvanostatic charge/discharge current at lower rate cycling, leading to diminished the electrochemical oscillation period in the LTO electrode at lower charge/discharge rates.

Based on the electrochemical performance summarized in Figure 2 and confirmed by electrochemical oscillation analysis, it is clear that the properly surface treated LTO thin film electrode which does not exhibit electrochemical oscillations has better long-term cycling stability, rate performance, and improved charge transfer. Thus, we suggest that the observed electrochemical oscillations provide a key indicator that can be used to evaluate the lithium-ions transportation/redistribution capability and phase separation kinetics in a multi-particle system, as well as to directly reveal bulk electrode-scale inhomogeneities. Nevertheless, it should be noted that the effects of the partially irreversible insulator-to-metal phase transition ( $\text{Li}_4\text{Ti}_5\text{O}_{12} \rightarrow \text{Li}_7\text{Ti}_5\text{O}_{12}$ ) during the first discharge has not been considered in this work. The residual metallic  $\text{Li}_7\text{Ti}_5\text{O}_{12}$  phase could also boost the rapid redistribution of both  $\text{Li}^+$  and electrons among/inside the electrode grains,<sup>[45,46]</sup> and thereby inducing phase-separation out of the equilibrium path. Additionally, the local accumulation of strain/defect at crystal grain boundaries has been observed to generate strain-enhanced ion/electrode transportation channels.<sup>[47,48]</sup> Since the grain boundary density of the polycrystalline LTO thin-film electrode is higher than the LTO composite electrode, complete understanding of the interplay between

electrochemical oscillations and battery performance should also include the consideration of the grain boundaries. These fundamental scientific issues underpin the success or failure of surface coating techniques for improving the performance of phase separation LIB materials yet they are not well understood. Both the effects of AZO surface coatings on discrete phase-separating behavior in a multi-particle LTO composite electrodes, and the correlation of this surface coating with near surface crystal structure relaxation,<sup>[21]</sup> require further in-depth studies.

### 3. Conclusions

To elucidate the critical role of surface modification layers on the batteries electrochemical performance, LTO thin-film electrodes with and without AZO nano-coating layers were constructed as experimental models to study of the underlying mechanisms of performance improvement. The effects of the self-sacrificing AZO modification layer on the electrochemical performance of deep-delithiated LTO thin-film electrodes were studied. We show that the electrochemical reaction between Li and AZO during initial discharge/charge process generates an efficient and high performance artificial SEI protection layer. The nano-mechanics and chemical compositions of this SEI layer were characterized using advanced *operando* SFMM spectra and post-mortem XPS, which confirms that in AZO(60)-LTO this thin SEI layer is highly homogeneous, mainly consisting of stiff, high elastic moduli and negligible viscosity inorganic components (Li-Zn alloy,  $\text{Li}_2\text{CO}_3$  and LiF). This artificial inorganic SEI layer has high ionic conductivity, protecting the electrode surface from electrolyte decomposition, and therefore dramatically improving the cycling and rate performance of the LTO anode. KPFM measurements suggested that the suppressed reduction kinetic on the EEI is key for the initial formation of the “self-sacrificing” SEI layer. Most importantly, by introducing this artificial SEI layer, we also demonstrate that surface modifications can not only modulate the surface conductivity and reductive capability, but also improve  $\text{Li}_7\text{Ti}_5\text{O}_{12} \rightleftharpoons \text{Li}_4\text{Ti}_5\text{O}_{12}$  phase transition kinetics through inhibiting the intrinsic electrochemical oscillations. This unambiguously suggests that the surface lithium wetting effect, as well as the rapid redistribution of lithium ions between the nano-grains are critical factors for the observation of electrochemical oscillations. Importantly, we attributed the enhanced electrochemical performance of the surface modified LTO electrodes to the suppressed electrochemical oscillations which represents a more homogenous local exchange current and intercalation/deintercalation states within the electrodes. This work highlights the importance of in-depth understanding of the enhancement mechanisms for electrode surface coatings in batteries, as well as filling an important gap between experimental observations and fundamental understanding of Li intercalation in multiparticle-phase-separating systems.

## 4. Experimental Section

### 4.1. Thin-film electrode preparations

LTO thin-film electrodes were deposited using RF magnetron sputtering. The deposition chamber was evacuated using a turbo-molecular pump to an initial pressure of  $4 \times 10^{-4}$  Pa, and the sample/target distance was fixed at 10 cm. LTO thin-film electrodes were deposited onto stainless steel (SS) substrates with a diameter of 15.5 mm.

During the deposition, the substrate temperature was kept at room temperature; the chamber pressure was maintained at 1.0 Pa. The gas flow rate was set at 50 sccm with Ar : O<sub>2</sub> = 4:1. The sputtering was conducted at a power of 120 W for 8 hours. After deposition, the LTO thin films were *in-situ* annealed at 700 °C for two hours. A ZnO target with a 2% aluminum doping rate was chosen as the modification material. Whereas ZnO is a wide-band gap semiconductor with low conductivity, its resistance is dramatically reduced by n-type aluminum doping. Additionally, besides the highly ionically conductive Zn-F phase, the by-product, AlF<sub>3</sub>, deriving from the AZO coating layer, could also improve the lithium interface compatibility, and therefore enhancing the long term cycling stability. AZO modification layers were directly deposited onto the annealed LTO thin-films surface under a sputtering pressure of 0.5 Pa and a flow rate of 22 sccm. The AZO layer thickness was controlled by varying the deposition times (30, 60 and 90 seconds), and the obtained composite AZO/LTO films are labelled as AZO(30)-LTO, AZO(60)-LTO, AZO(90)-LTO, respectively.

#### 4.2. Thin film structure characterizations

The sample crystal structures were determined by X-ray diffraction (XRD) (Rigaku Ultima IV, Cu K<sub>α1</sub> radiation, λ=0.15406 nm) and Raman spectroscopy. The surface compositions were analyzed by X-ray photoelectron spectrometer (XPS) (Thermo ESCALAB XI+). The surface and cross-section morphologies were characterized by scanning electron microscope (SEM) (Hitachi SU-8010) and scanning transmission electron microscope (STEM) (FEI Titan G2 80-200). STEM-EDS mapping was used to confirm the elemental distributions. AFM based measurements were carried out in Bruker Dimension Icon and Multimode. Kelvin probe force microscopy (KPFM) was used to measure the sample effective work function. Nano-electronic properties of LTO, AZO(30)-LTO, AZO(60)-LTO, AZO(90)-LTO were measured by conductive atomic force microscopy (C-AFM). *Operando* SFMM was performed using advanced vibration modulated mode [49-51] on a homemade ultrasonic SPM cell, as illustrated in Figure S1 in the SI.

#### 4.3. Electrochemical measurements

Annealed LTO and AZO-LTO composite thin films were assembled into 2025 coin-cells as the working electrodes. The calculation of the capacity contribution from the AZO coating layers can be found in the SI section 6. Li foils were chosen as the reference/counter electrodes. 1 M LiPF<sub>6</sub> in the mixture solution of ethylene carbonate (EC), diethyl carbonate (DEC) and dimethyl carbonate (DMC) (1: 1: 1 vol%) was used as the electrolyte. The half cells were charged/discharged at constant current using LAND CT2001A battery testing system with the cutoff voltages of 0.1-3.0 V at room temperature and 60 °C. Cyclic voltammetry (CV) tests were performed using an electrochemical workstation (Arbin Instruments BT2000, USA) with a scanning rate of 0.1 mV s<sup>-1</sup>. The electrochemical impedance spectra (EIS) were measured using a Zahner Zennium IM6 electrochemical workstation

in the frequency range of 100 mHz~100 kHz.

## Acknowledgments

The authors wish to acknowledge the financial support by the Natural Science Foundations of China (No. 61574037), Fujian Natural Science Foundation for Distinguished Young Scholars (Grant No. 2020J06042), Natural Science Foundation of Fujian Province (Grant No. 2018J01660), the Faraday Institution (grant number FIRG018), EU Graphene Flagship Core 3 project and EPSRC project EP/V00767X/1 and EP/P009050/1. This work was supported by the Henry Royce Institute for Advanced Materials, funded through EPSRC grants EP/R00661X/1, EP/S019367/1, EP/P025021/1 and EP/P025498/1.

## Author Contributions

<sup>†</sup> Y. Chen and HD. Pan contributed equally.

## Conflict of Interest

The authors declare no conflict of interest.

## References

- [1] X. Yu, A. Manthiram, *Energy Environ. Sci* **2018**, 11, 527.
- [2] C. Yan, R. Xu, Y. Xiao, J. F. Ding, L. Xu, B. Q. Li, J. Q. Huang, *Adv. Funct. Mater.* **2020**, 30, 1909887.
- [3] G. Sun, C. Zhao, F. D. Yu, R. Yu, J. Wang, J. Zhou, G. Shao, X. Sun, Z. B. Wang, *Nano Energy* **2021**, 79, 105459.
- [4] K. Pan, L. Zhang, W. Qian, X. Wu, K. Dong, H. Zhang, S. Zhang, *Adv. Mater.* **2020**, 32, 2000399.
- [5] K. M. Colbow, J. R. Dahn, R. R. Haering, *J. Power Sources* **1989**, 26, 397.
- [6] S. Scharner, W. Weppner, P. Schmid-Beurmann, *J. Electrochem. Soc.* **1999**, 30, 857.
- [7] D. Li, Y. Sun, Z. Yang, L. Gu, Y. Chen, H. Zhou, *Joule* **2018**, 2, 1265.
- [8] A. R. Iarchuk, V. A. Nikitina, E. A. Karpushkin, V. G. Sergeev, E. V. Antipov, K. J. Stevenson, A. M. Abakumov, *ChemElectroChem* **2019**, 6, 5090.
- [9] Y. Li, H. Chen, K. Lim, H. D. Deng, J. Lim, D. Fraggedakis, P. M. Attia, S. C. Lee, N. Jin, J. Moškon, Z. Guan, W. E. Gent, J. Hong, Y. S. Yu, M. Gaberšček, M. S. Islam, M. Z. Bazant, W. C. Chueh, *Nat. Mater.* **2018**, 17, 915.
- [10] L. Savignac, J. M. Griffin, S. B. Schougaard, *J. Phys. Chem. C* **2020**, 124, 7608.
- [11] P. Bai, D. A. Cogswell, M. Z. Bazant, *Nano Lett.* **2011**, 11, 4890.
- [12] K. Y. Park, J. Hong, W. M. Seong, J. J. Kim, K. Ku, B. Lee, K. Kang, *Energy Environ. Sci* **2017**, 10, 2352.
- [13] Y. B. He, F. Ning, B. Li, Q. S. Song, W. Lv, H. Du, D. Zhai, F. Su, Q. H. Yang, F. Kang, *J. Power Sources* **2012**, 202, 253.
- [14] D. Ahn, X. Xiao, *Electrochem. Commun.* **2011**, 13, 796.

- [15] D. Lei, H. Ye, C. Liu, D. An, J. Ma, W. Lv, B. Li, F. Kang, Y. B. He, *ACS Appl. Mater. Interfaces* **2019**, 11, 29993.
- [16] Y. Jin, H. Yu, Y. Gao, X. He, T. A. White, X. Liang, *J. Power Sources* **2019**, 436, 226859.
- [17] Y. Wang, Y. Ren, X. Dai, X. Yan, B. Huang, J. Li, *Royal Soc. Open Sci.* **2018**, 5, 180762.
- [18] W. Li, D. M. Lutz, L. Wang, K. J. Takeuchi, A. C. Marschlok, E. S. Takeuchi, *Joule* **2020**.
- [19] F. Huang, J. Ma, H. Xia, Y. Huang, L. Zhao, S. Su, F. Kang, Y. B. He, *ACS Appl. Mater. Interfaces* **2019**, 11, 37357.
- [20] S. Ganapathy, M. Wagemaker, *ACS Nano*. **2012**, 6, 8702.
- [21] H. C. Chiu, X. Lu, J. Zhou, L. Gu, J. Reid, R. Gauvin, K. Zaghib, G. P. Demopoulos, *Adv. Energy Mater.* **2017**, 7, 1601825.
- [22] H. Q. Dai, H. Xu, Y. N. Zhou, F. Lu, Z. W. Fu, *J. Phys. Chem. C* **2012**, 116, 1519.
- [23] Z. Lin, Y. Yang, J. Jin, L. Wei, W. Chen, Y. Lin, Z. Huang, *Electrochim. Acta* **2017**, 254, 287.
- [24] J. Deng, Z. Lu, C. Y. Chung, X. Han, Z. Wang, H. Zhou, *Appl. Surf. Sci.* **2014**, 314, 936.
- [25] H. Pan, Y. Chen, W. Pang, H. Sun, J. Li, Y. Lin, O. Kolosov, Z. Huang, *MethodsX* **2021**, 8, 101250.
- [26] B. A. Smith, B. Tolloczko, J. G. Martin, P. Grutter, *Biophys. J.* **2005**, 88, 2994.
- [27] K. Yamanaka, H. Ogiso, O. Kolosov, *Jpn. J. Appl. Phys.* **1994**, 33, 3197.
- [28] O. Piétrement, M. Troyon, *Surf. Interface Anal.* **2001**, 31, 1060.
- [29] P. Peljo, H. H. Girault, *Energy Environ. Sci* **2018**, 11, 2306.
- [30] W. Song, E. S. Scholtis, P. C. Sherrell, D. K. Tsang, J. Ngiam, J. Lischner, S. Fearn, V. Bemmer, C. Mattevi, N. Klein, F. Xie, D. J. Riley, *Energy Environ. Sci* **2020**, 13, 4977.
- [31] C. Yan, H. R. Li, X. Chen, X. Q. Zhang, X. B. Cheng, R. Xu, J. Q. Huang, Q. Zhang, *J. Am. Chem. Soc.* **2019**, 141, 9422.
- [32] B. Zhu, N. Liu, M. McDowell, Y. Jin, Y. Cui, J. Zhu, *Nano Energy* **2015**, 13, 620.
- [33] Q. Li, H. Pan, W. Li, Y. Wang, J. Wang, J. Zheng, X. Yu, H. Li, L. Chen, *ACS Energy Lett.* **2018**, 3, 2259.
- [34] J. Qian, L. Liu, J. Yang, S. Li, X. Wang, H. L. Zhuang, Y. Lu, *Nat. Commun.* **2018**, 9, 1.
- [35] X. Ran, J. Tao, Z. Chen, Z. Yan, Y. Yang, J. Li, Y. Lin, Z. Huang, *Electrochim. Acta* **2020**, 353, 135959.
- [36] Y. Liu, T. Zhou, Y. Zheng, Z. He, C. Xiao, W. K. Pang, W. Tong, Y. Zou, B. Pan, Z. Guo, Y. Xie, *ACS nano* **2017**, 11, 8519.
- [37] Q. Li, Y. H. Zhao, H. D. Liu, P. D. Xu, L. T. Yang, K. Pei, Q. W. Zeng, Y. Z. Feng, P. Wang, R. C. Che, *ACS Nano* **2019**, 13, 11921.
- [38] S. S. Li, X. B. Zhao, Y. Z. Feng, L. T. Yang, X. F. Shi, P. D. Xu, J. Zhang, P. Wang, M. Wang, R. C. Che, *Small* **2019**, 15, 1901343
- [39] B. Orvananos, T. R. Ferguson, H. C. Yu, M. Z. Bazant, K. Thornton, *J. Electrochem. Soc.* **2014**, 161, A535.
- [40] C. Tian, Y. Xu, D. Nordlund, F. Lin, J. Liu, Z. Sun, Y. Liu, M. Doeff, *Joule* **2018**, 2, 464.
- [41] B. C. Han, A. Van der Ven, D. Morgan, G. Ceder, *Electrochim. Acta* **2004**, 49, 4691.
- [42] W. Dreyer, J. Jamnik, C. Guhlke, R. Huth, J. Moškon, M. Gaberšček, *Nat. Mater.* **2010**, 9, 448.

- [43] W. C. Chueh, F. El Gabaly, J. D. Sugar, N. C. Bartelt, A. H. McDaniel, K. R. Fenton, K. R. Zavadil, T. Tyliczszak, W. Lai, K. F. McCarty, *Nano lett.* **2013**, 13, 866.
- [44] Y. Li, F. El Gabaly, T. R. Ferguson, R. B. Smith, N. C. Bartelt, J. D. Sugar, K. R. Fenton, D. A. Cogswell, A. L. D. Kilcoyne, T. Tyliczszak, M. Z. Bazant, W. C. Chueh, *Nat. Mater.* **2014**, 13, 1149.
- [45] C. Kim, N. S. Norberg, C. T. Alexander, R. Kostecki, J. Cabana, *Adv. Funct. Mater.* **2013**, 23,1214.
- [46] M. S. Song, A. Benayad, Y. M. Choi, K. S. Park, *Chem. Commun.* **2012**, 48, 516.
- [47] L. T. Yang, X. Z. Zhu, X. H. Li, X. B. Zhao, K. Pei, W. B. You, X. Li, Y. J. Chen, C. F. Lin, R. C. Che, *Adv. Energy Mater.* **2019**, 9, 1902174.
- [48] W. L. Jiao, C. Chen, W. B. You, X. R. Zhao, J. Zhang, Y. Z. Feng, P. Wang, R. C. Che, *Adv. Energy Mater.* **2020**, 10, 1904072.
- [49] B. J. Robinson, M. E. Pumarol, O. V. Kolosov, *Physical Review B* **2019**, 100, 235426.
- [50] B. J. Robinson, N. D. Kay, O. V. Kolosov, *Langmuir* **2013**, 29, 7735.
- [51] O. V. Kolosov, M. R. Castell, C. D. Marsh, G. A. D. Briggs, T. I. Kamins, R. S. Williams, *Phys. Rev. Lett.* **1998**, 81, 1046.

## Supporting Information

### Controlling interfacial reduction kinetics and suppressing electrochemical oscillations in the $\text{Li}_4\text{Ti}_5\text{O}_{12}$ thin-film anode

*Yue Chen,<sup>1,2,†</sup> Handian Pan,<sup>1,3,†</sup> Chun Lin,<sup>1,3</sup> Jiaxin Li,<sup>1,3\*</sup> Rongsheng Cai,<sup>4</sup> Sarah J. Haigh,<sup>4</sup> Guiying Zhao,<sup>1,5</sup> Jianmin Zhang,<sup>1\*</sup> Yingbin Lin,<sup>1,5</sup> Oleg V. Kolosov,<sup>2\*</sup> and Zhigao Huang<sup>1,5\*</sup>*

<sup>1</sup>College of Physics and Energy, Fujian Normal University, Fujian Provincial Key Laboratory of Quantum Manipulation and New Energy Materials, Fuzhou, 350117, China

<sup>2</sup>Physics Department, Lancaster University, LA1 4YB, UK

<sup>3</sup>Fujian Provincial Engineering Technical Research Centre of Solar-Energy Conversion and Stored Energy, Fuzhou, 350117, China

<sup>4</sup>Department of Materials, University of Manchester, Manchester, M13 9PL, UK

<sup>5</sup>Fujian Provincial Collaborative Innovation Center for Advanced High-Field Superconducting Materials and Engineering, Fuzhou, 350117, China

# 1. Shear Force Modulation Microscopy (SFMM) and three-dimensional (3D) nano-rheology.

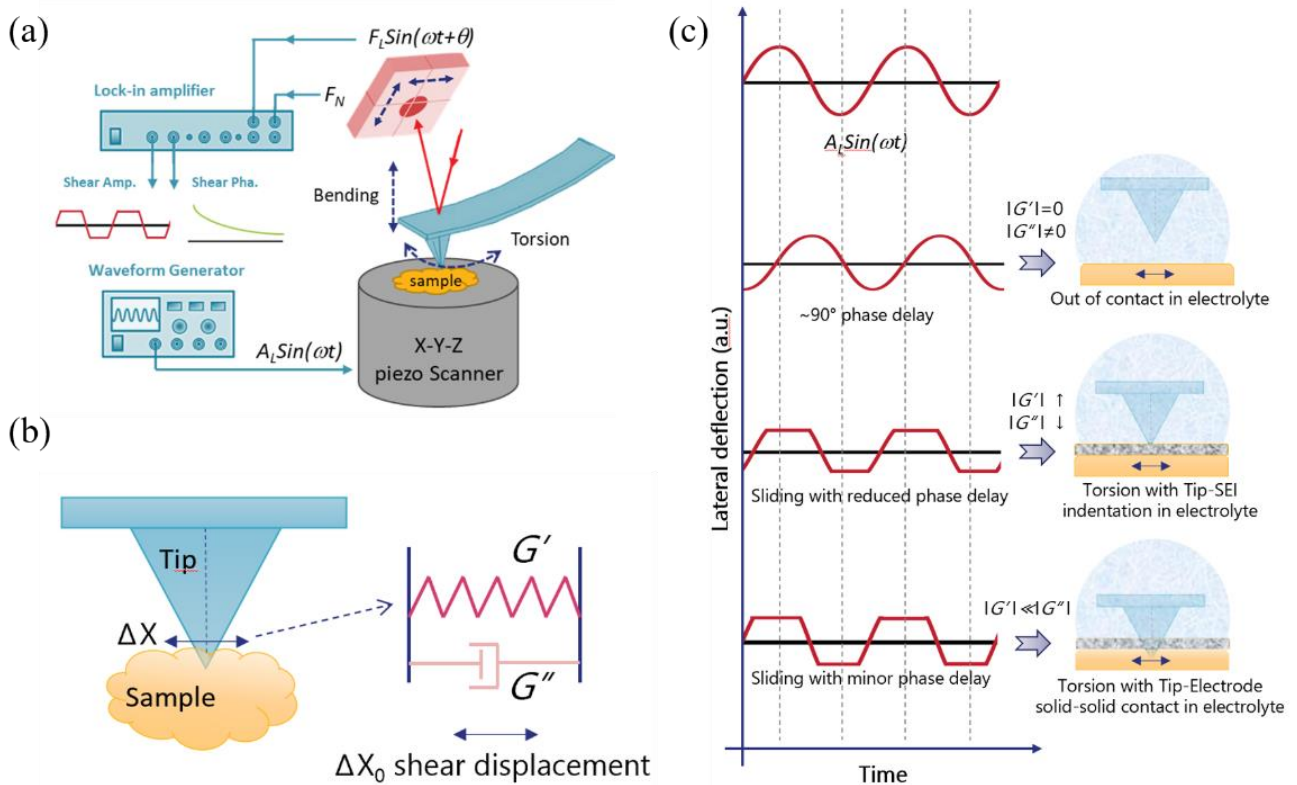


**Figure S1.** (a) The diagram of SFMM, (b) the tip-sample contact model and (c) analysis of phase delay during the tip approaching processes.

A home-made atomic force microscope (AFM) with a custom-made signal breakout box was adapted for SFMM as illustrated in Figure S1 (a). A sinusoidal drive signal  $A_L \sin(\omega t)$  with a tunable frequency of 0.6-2.0 kHz, well below the tip resonance frequency, is applied to the Y direction of a piezo-tube scanner via in-line audio transformer to dither the sample laterally causing lateral force applied to the AFM tip. Typically, the peak-to-peak amplitude  $A_L$  of the drive signal was set around 10-60 mV applied counter in counter phase to the AFM tube scanner (Bruker Multimode, large area scanner), which corresponds to a nominal lateral sample deflection of around 2-12 nm. The amplitude and phase shift of the cantilever lateral oscillation (torsion) response were measured with a lock-in amplifier. Approach and retract curves were captured at a rate of 0.02 Hz, with a Z-ramp of 500 nm. For torsion phase mapping, the drive amplitude was selected at the ‘tip-sample sliding region’ by slowly increasing applied voltage until the ‘sliding’ could be observed in the lateral deflection signal <sup>[1]</sup>. As the torsional signal phase changes from  $90^\circ$  in the liquid electrolyte to  $0^\circ < \theta < 90^\circ$  in the gel-like solid-electrolyte interphase (SEI) to  $0^\circ$  in the solid-solid contact, during the imaging it was possible to keep the vertical deflection in the tip-SEI indentation region by setting the deflection set-point corresponding to the  $0^\circ < \theta < 90^\circ$  torsion phase delay.

Under different indentation depths, precise estimation of the tip-sample contact mechanics regime is the major challenge for determining which contact mechanics regime is appropriate for SFMM.<sup>[2,3]</sup> In this measurement, we were focusing on identifying the existence of SEI layer and its thickness on LTO and AZO decorated LTO surface, rather than quantifying the SEI nano-mechanical properties. Therefore, torsional phase, which is sensitive to the sample viscoelasticity, is the critical parameter that was used for SEI detection in this SFMM measurement. According to previous reports on nano-rheology,<sup>[4]</sup> as

shown in Figure S1 (b), the shear vibration of the tip-sample junction can be simply separated into two components, the energy storage and the energy loss, which directly relate to the materials' storage modulus  $G'$  and loss modulus  $G''$ , respectively. The energy storage component dominates when the tip and sample are in solid-solid contact, while the loss modulus component, which is related to the dissipated heat and electrolyte/SEI viscous caused hysteresis, takes over when the tip is contacting a soft/viscous material. The phase ( $\theta$ ) of lateral deflection signal  $F_L = \sin(\omega t + \theta)$  provides the critical information on the tip-sample contact status in which:

$$\theta = \arctan \frac{|G''|}{|G'|} \quad (1)$$

where  $G'$  and  $G''$  are the real and imaginary part of sample surface complex shear modulus ( $G^*$ ), respectively. According to this equation, phase-lag can be used to determine the tip-sample contact status, and therefore to semi-quantitatively map the mechanical properties of the SEI layers.

## 2. Phase delay analysis

In fact, phase measurement helps to monitor the sample displacement with very high vertical resolution down to the nm length scale. With a drive signal  $A_L \sin(\omega t)$  was applied, the tip torsion clearly varies at different tip-sample contact status, as shown in Figure S1 (c).

1. When the tip is out of contact with the sample surface in the electrolyte, the viscosity of the electrolyte contributes to the  $G''$  component, while the  $G'$  component is equal to 0, which results in a  $\sim 90$ -degree phase delay in the tip torsional deflection.
2. However, as the tip get closer to the sample surface, the tip torsional phase changes as long as it is pressed into the top SEI layer. In this case, the elastic modulus  $G'$  component starts to increase reducing the phase lag. In our measurements, the high modulation amplitudes (about 5 nm) cause tip sliding on the surface, the lateral force reaches the limiting friction force, and the torsional signal becomes a nearly rectangular signal<sup>[1]</sup>. It is worth noting that, at low vertical displacement, the tip might stick to the sample and there is no phase lag, whereas when the tip slides on the surface, the phase decreases and then becomes a constant,<sup>[5]</sup> and independent on the sample properties, this is the reason why our SFMM need to work in the sliding region rather than the static friction region.
3. When the SEI layers were totally penetrated by the tip (or the tip reaches the inorganic underlying SEI layer) with a solid-solid contact, the tip sticks to the sample surface, and the elastic component becomes dominating compared to the viscoelasticity arising either from the SEI or the electrolyte ( $G'' \ll G'$ ), and thus the tip torsional displacement and lateral drive signals are approximately in phase. In summary, this approach of shear force phase measurement in SFMM provides both the 3D profile of the viscoelasticity profile of the electrode surface layers in each point, hence the name of "3D nano-rheology".

## 3. XRD characterization

**Table S1** Diffraction peaks identified in the XRD patterns of bare LTO thin film

Miller indices (h k l)	Peak position $2\theta$ ( $^\circ$ )	Spacing (nm)
1 1 1	18.26	0.484
3 1 1	35.44	0.252
4 0 0	43.10	0.209
3 3 3	57.12	0.161
4 4 0	62.68	0.148

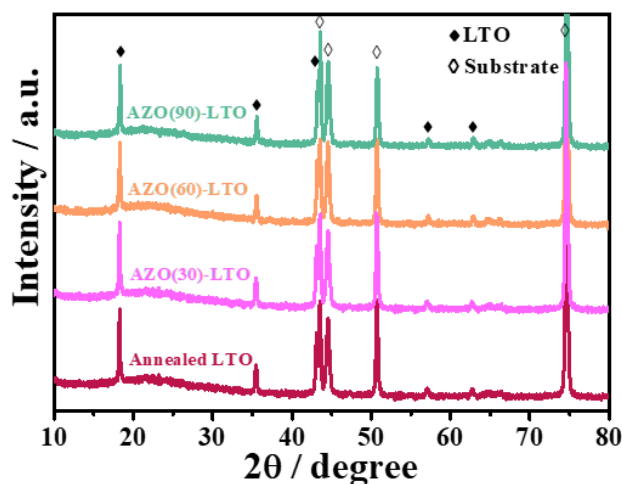
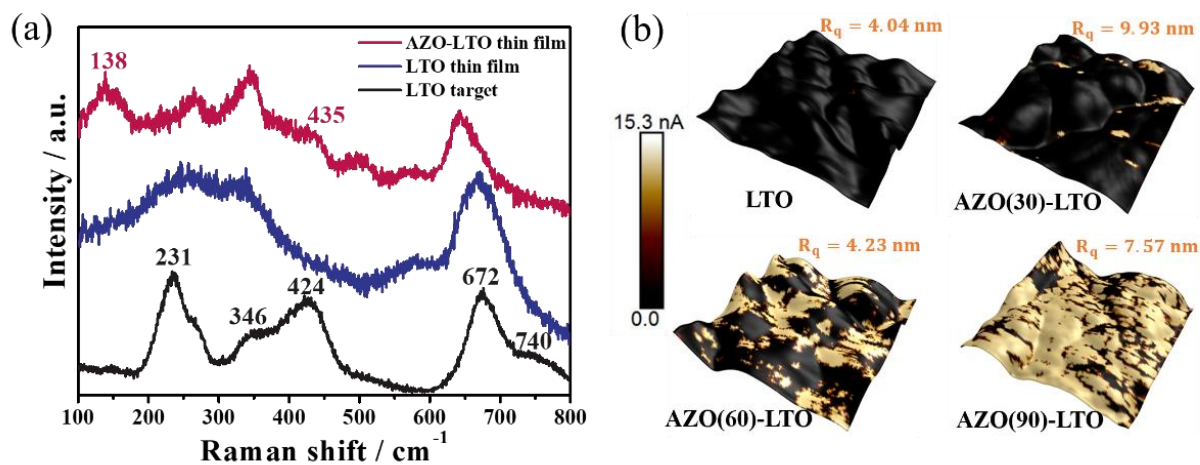
**Figure S2** XRD patterns of annealed LTO and AZO-LTO thin-films with different AZO coatings (treated for different surface sputtering times).

Figure S2 is the XRD patterns of annealed LTO and AZO-LTO thin-films treated with the different surface sputtering time. No extra peaks were present in the AZO-LTO compared to bare LTO. This may be due to either the low thickness, or the amorphous structure of these AZO nano-layers. Therefore, we further characterized these ultra-thin AZO coating layers by using Raman spectroscopy and conductive atomic force microscopy (C-AFM), as shown in Figure S3 and TEM (Figure S5).

#### 4. Raman and conductive AFM (C-AFM) characterization

As seen in Figure S3 (a), five vibration peaks at 231, 346, 425, 674 and 740  $\text{cm}^{-1}$  are found in the spectrum of the LTO target. The two higher frequency bands (674 and 740  $\text{cm}^{-1}$ ) are assigned to the vibrations of Ti-O bonds in  $\text{TiO}_6$  octahedra.<sup>[6]</sup> The middle frequency bands (346 and 425  $\text{cm}^{-1}$ ) correspond to the Li-O bond vibrations in the  $\text{LiO}_4$  and  $\text{LiO}_6$  polyhedra, respectively. Similarly, for annealed LTO and AZO(60)-LTO films, two vibrational peaks located at 346 and 674  $\text{cm}^{-1}$  are found, indicating that stoichiometric LTO films have been successfully grown on the SS current collector. Additionally, for the AZO(60)-LTO film, two extra vibrational peaks at wave numbers of 138 and 435  $\text{cm}^{-1}$  can be attributed to the  $\text{ZnO}$   $E_2$  (low) and (high) modes located at around 100  $\text{cm}^{-1}$  and 438  $\text{cm}^{-1}$ ,<sup>[7,8]</sup> which proves that the AZO layer has been deposited on the LTO film.



**Figure S3** (a) Raman spectrum of LTO target, LTO and AZO(60)-LTO thin-film; (b) 3D topography rendering with superimposed color C-AFM contrast (bright color corresponds to higher electrical conductance) images of LTO, AZO(30)-LTO, AZO(60)-LTO and AZO(90)-LTO thin-films. (C-AFM was measured by applying a 6 V constant voltage to the sample current collector and detecting the current flowing through the conductive tip at each image pixel using Gamry Reference-600 potentiostat current monitor).

Figure S3 (b) shows C-AFM measurement results of LTO and AZO modified LTO, where the 3D topographical AFM images rendered with C-AFM current intensity represented by color. The brighter areas have higher electronic conductance, while the darker areas are less conductive. From Figure S3 b, it can be seen that the bare LTO film has no current response (low conductivity). For the AZO(30)-LTO sample, there were some sporadic current signals located in the recesses between the LTO grains, which indicates that for the shorter sputtering time with 30 s, LTO film is only partially coated by AZO. With longer sputtering times, the coverage of the bright areas is significantly increased. For the AZO(60)-LTO thin film, the majority of the surface has been covered by AZO, which is consistent with the SEM and HR-TEM results. However, for the longer sputtering time of 90 s, most of the surface becomes bright, indicating continuous cover by conductive AZO.

## 5. SEM and TEM characterization

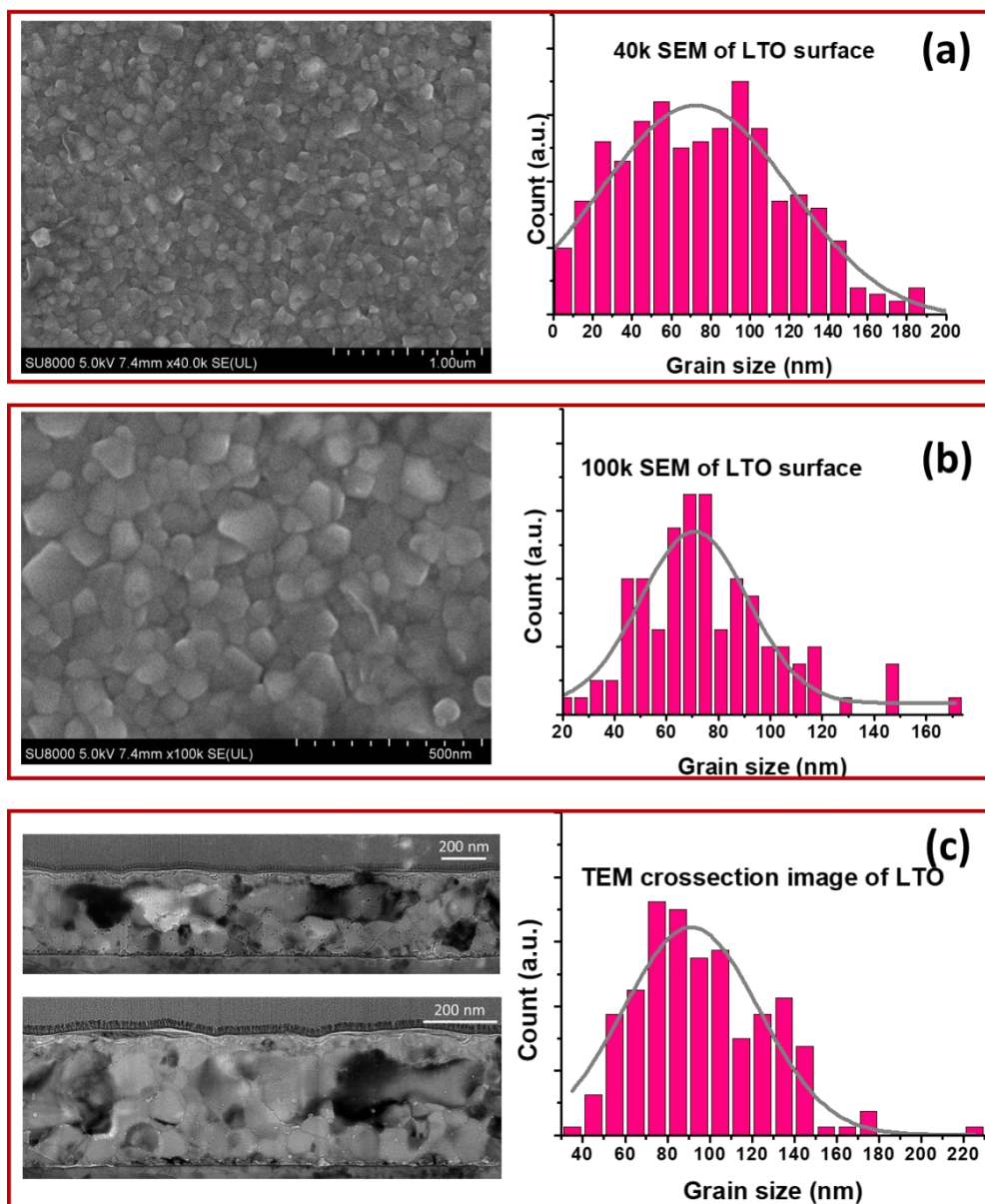


**Figure S4** (a, b) SEM imaging and © TEM of the LTO anodes and the respective measured grain size distributions.

We calibrate the LTO grain size both using the SEM images on sample surface and HRTEM images of sample cross-section (bulk). It can be found in Figure S4 (a) and (b), the SEM images with different magnifications both show that the mean surface grain size is 70 nm. However, the grain size distribution observed from the two cross-section HRTEM images in Figure S4 (c) reveals a slightly higher internal grain size of ~90 nm.

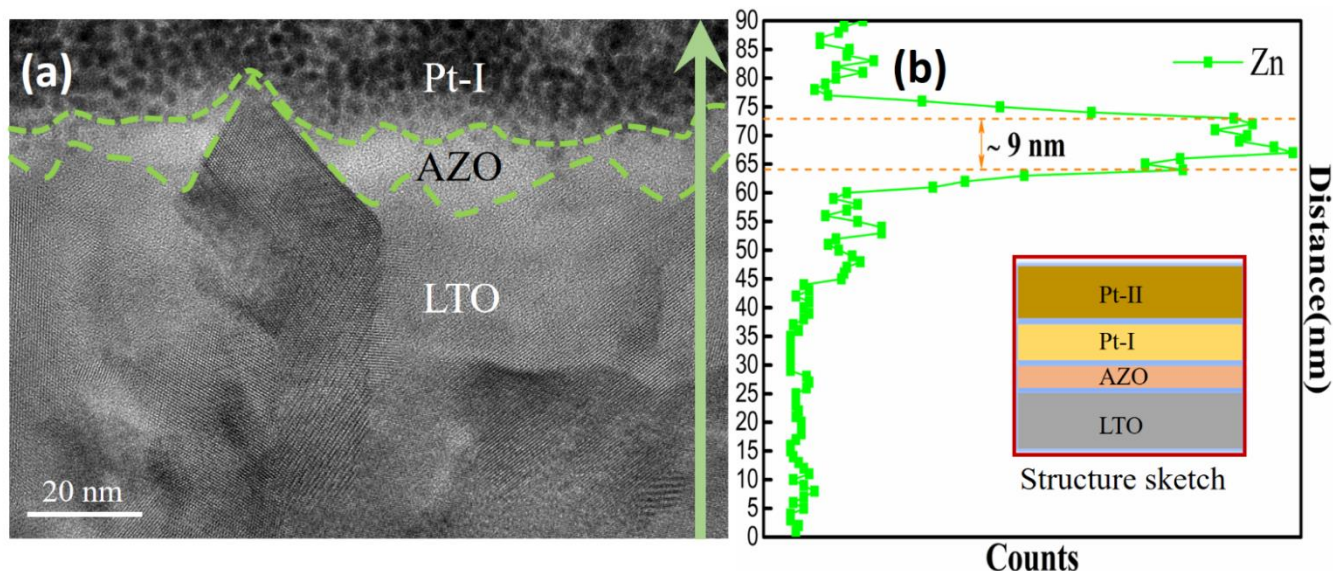


**Figure S5** (a) HRTEM image at LTO/AZO/Pt interfaces and (b) the Zn elemental line scan across the interfaces (inset is sketch of the sample structure); (c) HRTEM image of the AZO/Pt-I interfaces for the rectangular area in (d) cross-section TEM image; HRTEM image and corresponding Pt/Zn elemental map of (e) bare LTO and (f) AZO coated LTO thin-film electrode.

The FIB-Pt protection layers have two distinct types of structure (corresponding to the lower electron deposited layer, Pt-I, and the ion beam deposited layer, Pt-II). As the inset sketch shows in Figure S5 (b) indicates, the top lamella welding Pt layer (Pt-II) is a denser amorphous layer, while the Pt protection layer near the AZO surface (Pt-I) shows crystalline nano-cluster like structure (Figure S5 (c) and S4 (d)) which can be easily distinguished from the amorphous AZO layer. Moreover, the location of the AZO layer was confirmed by EDS elemental line scan, as shown in Figure S5 (b). By comparing the HAADF-STEM image and Pt/Zn mapping in AZO-coated LTO (Figure S5 (e)) and bare LTO samples (Figure S5 (f)), an obvious Zn signal “strip” can be found between the Pt and AZO-coated LTO surface, in which the amorphous part of AZO can be easily determined, while Zn signal represented only as background noise in the bare LTO samples.

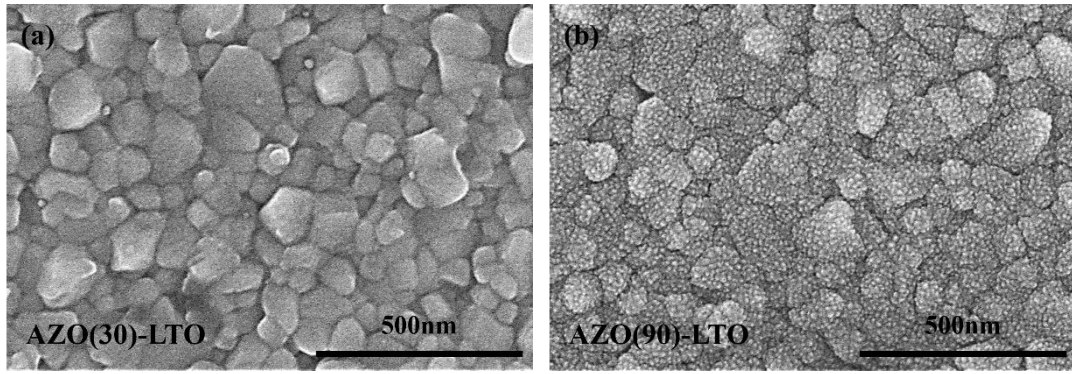


**Figure S6** Surface SEM images of (a) AZO(30)-LTO and (b) AZO(90)-LTO thin-films.

**Figures S6** (a) and (b) are the surface SEM images of AZO(30)-LTO and AZO(90)-LTO thin films, where it is seen that the AZO particular surface decoration becomes more visible with the increase of sputtering time.

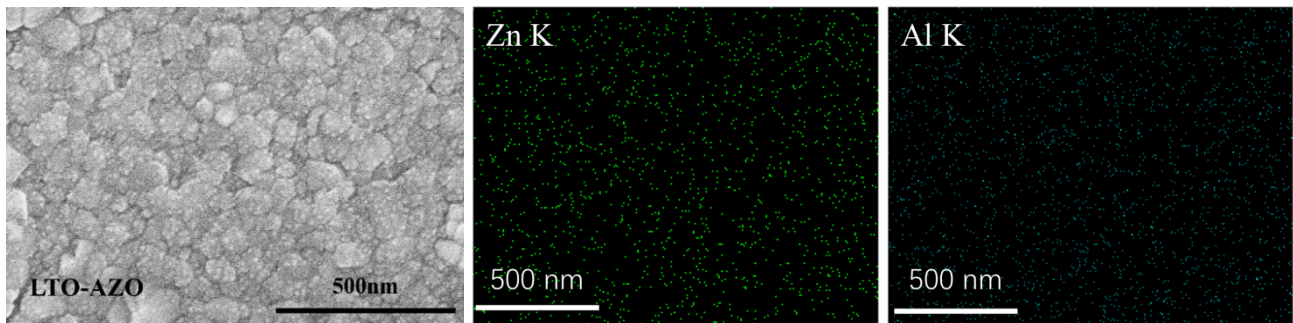


**Figure S7** SEM EDS elemental mapping of Zn and Al for the AZO(60)-LTO films.

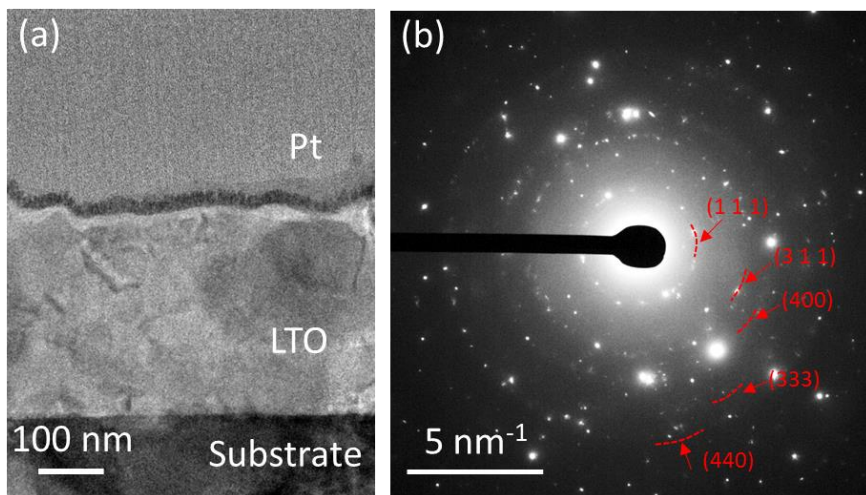


**Figure S8** (a) The TEM image indicating the SAED electron aperture position; (b) The SAED patterns acquired within the LTO region in Figure S8 (a).

The selected area electron diffraction (SAED) patterns are captured from within the LTO layer (Figure S8 (a)). As shown in Figures S8 (b), the electron diffraction patterns show polycrystalline diffraction rings with diameters of  $4.17 \text{ nm}^{-1}$ ,  $8.03 \text{ nm}^{-1}$ ,  $9.89 \text{ nm}^{-1}$ ,  $12.35 \text{ nm}^{-1}$  and  $13.70 \text{ nm}^{-1}$  corresponding to the LTO crystal planes (111), (311), (400), (333) and (440),

respectively (summarized in Table S2). These lattice-spacing values agree well with the TEM imaging (Figure 1g-j) and the XRD characterization (supporting information section 3). Moreover, no impurity diffraction signals can be found in the patterns, which further confirms that the synthesized LTO has high phase purity.

**Table S2** The summary of electron diffraction-ring diameters and corresponding crystal planes (measurement accuracy ~5%)

Diameter (nm <sup>-1</sup> )	Lattice spacing (nm)	Crystal plane
D1=4.167	0.480	(1 1 1)
D2= 8.032	0.249	(3 1 1)
D3= 9.893	0.202	(4 0 0)
D4=12.346	0.162	(3 3 3)
D5= 13.703	0.146	(4 4 0)

## 6. Electrochemical measurements

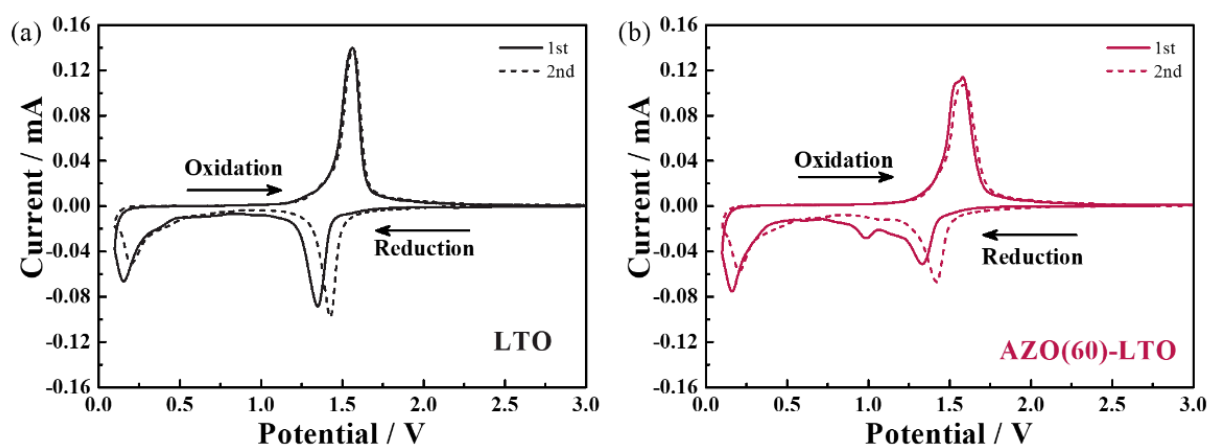


**Figure S9** CV curves of (a) LTO and (b) AZO(60)-LTO thin-film electrodes within 0.1~3.0 V at 0.1 mV s<sup>-1</sup>.

Previous reports have demonstrated that, by inserting lithium into lithium 48f sites, discharging Li<sub>4</sub>Ti<sub>5</sub>O<sub>12</sub> to 0.01 V vs lithium can release extra capacity<sup>[9,10]</sup> and even deliver 310 mAh/g upon the first discharge. In other words, the extra capacity below 1.0 V is about ~77% of the theoretical capacity when cycling between 3.0-1.0 V vs Li. This is also one of the main motivations of our research, that is to release the extra capacity within the deep lithiation voltage range while still inhibiting the SEI formation using AZO surface modification. Additionally, the capacity contribution of Zn reversible alloy reactions within this voltage range is relatively small compared to the reversible lithium intercalation in LTO active material. To be more specific, the average total weight of the LTO active material layer in each thin-film electrode is about 210-230 μg, whereas the theoretical capacity of LTO between 3.0-0.1 V vs lithium is 260 mAh/g, thus, the absolute capacity of the LTO thin-film electrode is about 54.6-58.9 μAh. The average thickness of AZO after 60 seconds sputtering is estimated to be 10 nm, the diameter of electrode is the 15.5 mm, AZO density is ~5.61 g/cm<sup>3</sup>, therefore the estimated mass of the AZO coating layer is around 10.6 μg. According to the literature, the theoretical capacity of AZO is about 600 mAh/g, therefore the absolute

capacity of the AZO coating is around 6.3  $\mu\text{Ah}$ . In this case, even if all of the AZO lithiation/de-lithiation is reversible, the capacity contribution is less than 10 %. However, as can be found in the cycling performance (Figure 2a of manuscript), the capacity retention of AZO(60)-LTO is more than 20% greater than the bare LTO after 300 cycles. In this work, we calculated the thin film electrode areal capacity by dividing the absolute capacity using the electrode area ( $\sim 1.885 \text{ cm}^2$ ), thus the theoretical areal capacity of a bare LTO thin film electrode is about 29.0-31.2  $\mu\text{Ah}/\text{cm}^2$ .

The first and second CV curves of the bare LTO and AZO(60)-LTO samples are shown in Figure S9. From the CV curves of bare LTO in Figure S9 (a), one can find two reduction peaks at around 1.45 V and 0.20 V, as well as one oxidation peak at around 1.55 V. The high voltage reduction peak corresponds to the process of the 3 Li atoms entering the 16c sites and the migration of Li from the original 8a sites to the 16c sites ( $[\text{Li}_3]^{8a}[\text{Li}_1\text{Ti}_5]^{16d}[\text{O}_{12}]^{32e} \rightarrow [\text{Li}_{0.16}]^{8a}[\text{Li}_1\text{Ti}_5]^{16d}[\text{Li}_{5.84}]^{16c}[\text{O}_{12}]^{32e}$ ); The lower reduction peak can be attributed to the transformation ( $[\text{Li}_{0.16}]^{8a}[\text{Li}_1\text{Ti}_5]^{16d}[\text{Li}_{5.84}]^{16c}[\text{O}_{12}]^{32e} \rightarrow [\text{Li}_{0.62}]^{8a}[\text{Li}_1\text{Ti}_5]^{16d}[\text{Li}_6]^{16c}[\text{Li}_{0.38}]^{48f}[\text{O}_{12}]^{32e}$ ). The oxidation peak should derive from the charge compensation by the  $\text{Ti}^{3+}/\text{Ti}^{4+}$  redox pair upon the extraction of lithium from the fully lithiated state LTO. Besides the additional reduction peak slightly below 1 V, the CV curves of AZO(60)-LTO show similar reduction and oxidation peaks as bare LTO. This additional peak should be attributed to the reduction of the AZO coating layer. Importantly, this reduction peak almost disappeared during the second voltage scan, indicating a robust “self-sacrificing” protecting layer was formed after the 1<sup>st</sup> cycle.

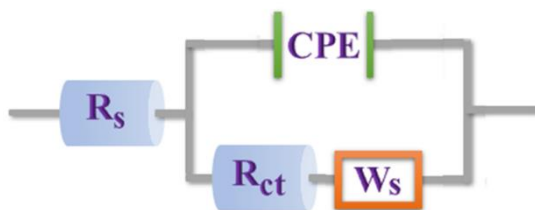


**Figure S10** Equivalent circuit model for EIS fitting.  $R_s$  and  $R_{ct}$  represent the system resistance (such as contact resistance and electrolyte resistance) and charge transfer resistance, respectively, CPE is constant phase element and  $W_s$  is Warburg diffusion element corresponding to lithium-ion diffusion.

Figure S10 is the Equivalent circuit model for the EIS spectra, the  $R_s$  and  $R_{ct}$  were determined by fitting the EIS spectra using ZSimpWin software. The fitting parameters are summarized the Table S3. As shown in Table S3, it is noted that the AZO-coated LTO cells all show lower charge transfer resistance compared to the bare LTO (1298  $\Omega$ ), with the AZO(60)-LTO cell having the lowest charge transfer after the 100<sup>th</sup> cycle ( $\sim 160 \Omega$ ). The chemical diffusion coefficient of  $\text{Li}^+$  ( $D_{\text{Li}^+}$ ) can be further calculated based on the relationship between the real axis ( $Z'$ ) and the reciprocal square root ( $\omega^{-1/2}$ ) at the low frequency region as follows<sup>[11]</sup>

$$Z' = R_e + R_{ct} + \sigma_\omega \omega^{-1/2} \quad (2)$$

$$D_{\text{Li}^+} = \left( \frac{2RT}{\sqrt{2}n^2F^2\sigma_\omega AC} \right)^2 = \frac{2R^2T^2}{n^4F^4\sigma_\omega^2A^2C^2} \quad (3)$$

where  $R$ ,  $T$  and  $F$  are gas constant, absolute temperature and Faraday's constant respectively,  $n$  is the number of electrons per molecule during oxidation,  $\sigma_\omega$  is Warburg coefficient,  $A$  is the surface area of the electrode,  $C$  is the molar volume of active material. According to the equations (2) and (3), the lithium diffusion constants ( $D_{\text{Li}^+}$ ) can be calculated by plotting the  $Z_{re}$  vs

$\omega^{-1/2}$  in the low frequency diffusion region as shown in Figure S11. One can find in Figure S11 that, after 100 cycles at room temperature and 1 C, the  $D_{Li^+}$  of LTO, AZO(30)-LTO, AZO(60)-LTO and AZO(90)-LTO electrodes are around  $3.30 \times 10^{-12} \text{ cm}^2 \text{ s}^{-1}$ ,  $6.81 \times 10^{-12} \text{ cm}^2 \text{ s}^{-1}$ ,  $3.12 \times 10^{-11} \text{ cm}^2 \text{ s}^{-1}$  and  $9.12 \times 10^{-12} \text{ cm}^2 \text{ s}^{-1}$ , respectively.

**Table S3** EIS fitting parameters of bare LTO and AZO coated LTO.

Parameters in Model: R(Q(RW))	Bare LTO	AZO(30)-LTO	AZO(60)-LTO	AZO(90)-LTO
$R_s$ (ohm)	3.382	2.945	2.543	2.646
CPE ( $S \cdot \text{sec}^n$ )	$1.270 \times 10^{-5}$	$1.383 \times 10^{-5}$	$1.695 \times 10^{-5}$	$1.484 \times 10^{-5}$
Freq. Power	$7.399 \times 10^{-1}$	$7.357 \times 10^{-1}$	$7.467 \times 10^{-1}$	$6.861 \times 10^{-1}$
$R_{ct}$ (ohm)	$1.298 \times 10^3$	$5.533 \times 10^2$	$1.597 \times 10^2$	$4.353 \times 10^2$
W ( $S \cdot \text{sec}^{0.5}$ )	$1.974 \times 10^{-4}$	$4.600 \times 10^{-4}$	$7.749 \times 10^{-4}$	$5.425 \times 10^{-4}$
Chsq	$1.604 \times 10^{-4}$	$1.313 \times 10^{-3}$	$4.529 \times 10^{-3}$	$5.734 \times 10^{-4}$
Average Std. error (%)	1.242	4.497	4.314	3.926

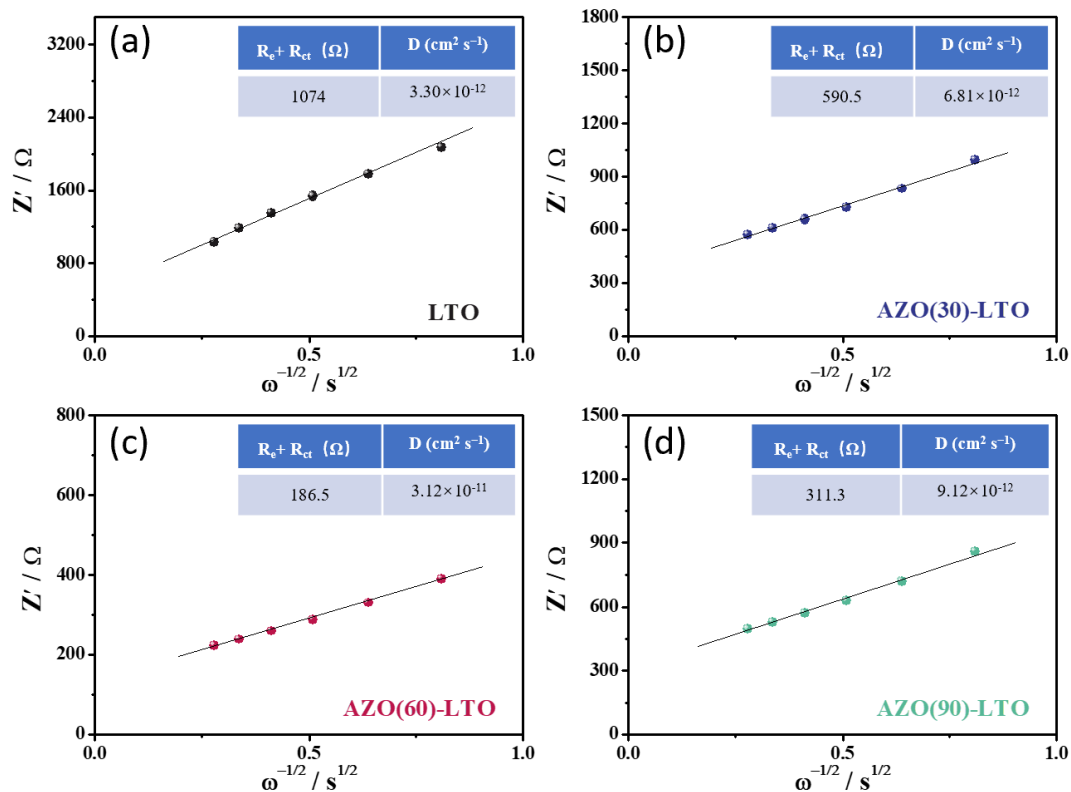


**Figure S11**  $Z_{re}$  plotted as a function of  $\omega^{-1/2}$  at low frequency diffusion region.

## 7. Effective work function (EWF) calculation

The KPFM system was introduced to determine the sample effective work function. We calculate the effective work function of the sample based the measured contact potential difference ( $V_{CPD}$ ) between the tip and the thin-film surface according to the following formula,

$$V_{CPD} = \frac{(\varphi_{tip} - \varphi_s)}{q}$$

where  $\varphi_{tip}$  and  $\varphi_s$  are the work function of the tip and the sample, respectively;  $q$  is the charge of the electron.  $\varphi_{tip}$  can be determined by testing a well-defined standard sample (such as Au/HOPG). In this calculation, we calibrated all sample effective work functions by setting the work function value of a sputtering gold surface as 5.2 eV.

## 8. XPS characterization on post-mortem thin-film electrodes

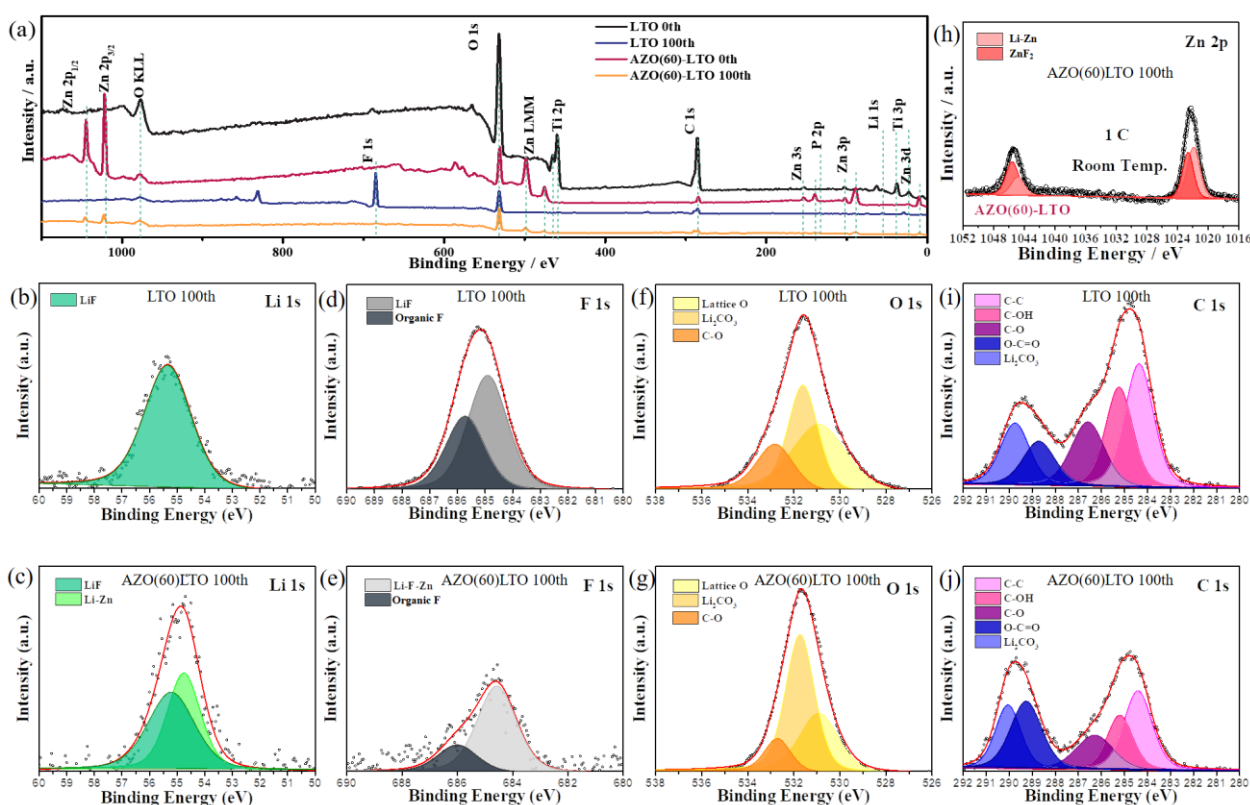


**Figure S12.** (a) Post-mortem XPS survey spectra of bare LTO and AZO(60)-LTO electrodes after the 100th cycle. (b-j) high-resolution spectra of (b)/(c) Li 1s, (d)/(e) F 1s, (f)/(g) O 1s and (i)/(j) C 1s peak of bare LTO/AZO(60)-LTO electrodes. (h) Zn 2p peak of AZO(60)-LTO electrodes.

We disassembled the batteries after cycling and then carried out XPS measurements on the electrode surface, with the results shown in Figure S12. Figure S12 (a) shows the XPS survey spectra of the pure LTO and AZO(60)-LTO electrodes after the 100<sup>th</sup> cycle. Comparing to the as-prepared sample, some additional elemental peaks, including fluoride, oxygen and carbon, can be found in the cycled samples. These peaks should be attributed to the organic/inorganic decomposition products

on the electrode surface. As shown in Figure S12 (a), a strong peak at  $\sim 685.2$  eV attributed to the fluoride <sup>[12]</sup> can be found in the LTO electrode after cycling, while the fluoride peak from the AZO(60)-LTO electrode is very weak. Additionally, from the high resolution XPS spectrum in Figure S12 (e), it can be seen that in AZO(60)-LTO the metallic fluoride 1s peak shifts to the lower binding energy region. It may be due to the different metallic fluoride decompositions (Li/Zn-F) in the SEI layer derived from the AZO coating. The peak fitting of Li 1s can be found in Figures S12 (b) and (c). One can observe that only one Li 1s peak at  $\sim 55.3$  eV is found in the bare LTO electrode surface, attributed to LiF; while an additional peak at  $\sim 54.8$  eV, corresponding to the Li-Zn alloy,<sup>[13]</sup> can be found in the AZO(60)-LTO samples. The existence of a Li-Zn alloy in AZO(60)-LTO is also proved by the metallic Zn 2p<sup>3/2</sup> and Zn 2p<sup>1/2</sup>,<sup>[14]</sup> as shown in Figure S12 (i). A closer examination of the O 1s peak in Figures S12 (f) and (g) shows that, compared to the bare LTO electrode, the AZO(60)-LTO electrode surface has a higher amount of inorganic (Li<sub>2</sub>CO<sub>3</sub>) but less organic C-O species. This agrees well with the measured C 1s spectra in Figures S12 (i) and (j), where higher C-OH, C-O and O-C=O species can also be found in the decomposition products of the bare LTO electrode surface. Therefore, post-mortem XPS analysis indicates that the SEI layers formed on the bare LTO surface may contain an organic oligomer, especially organic fluoride, mixed with inorganic LiF/Li<sub>2</sub>CO<sub>3</sub>, while the AZO coating layer was converted into Li/Zn-F inorganic reduction products which greatly reduced the formation of fluoride decomposition products. This is consistent with *operando* SFMM characterization which showed that a more mechanically homogenous layer was formed on the electrode surface with AZO nano-coating.

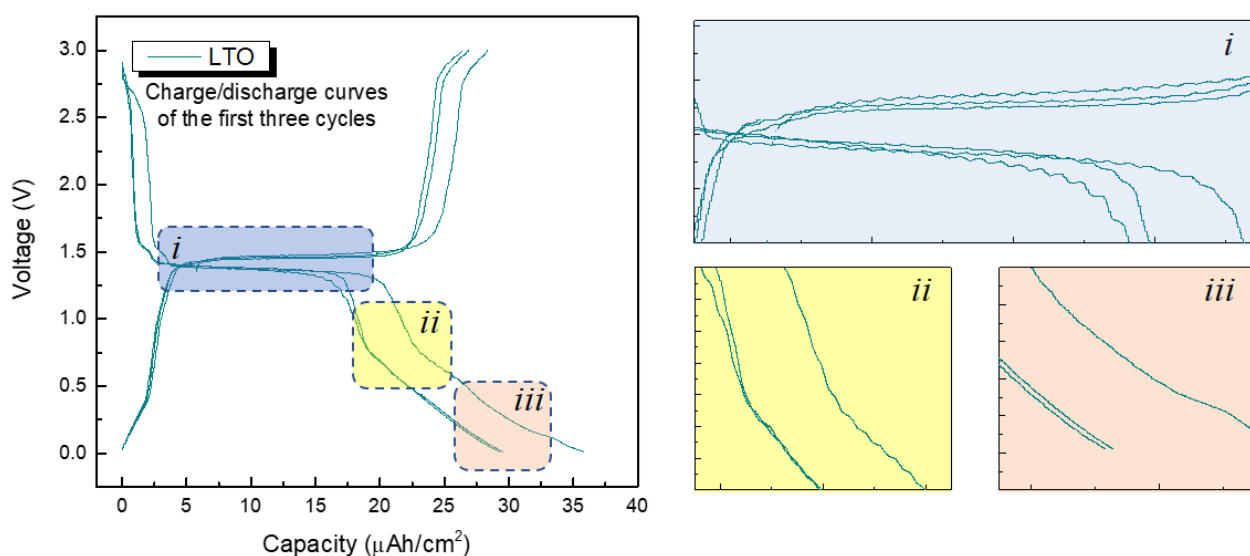


**Figure S13** voltage oscillation in LTO thin-film electrodes near the phase transition regions

## References

- [1] B. J. Robinson, M. E. Pumarol, O. V. Kolosov, *Physical Review B* **2019**, 100, 235426.
- [12] S. Ge, Y. Pu, W. Zhang, M. Rafailovich, J. Sokolov, C. Buenviaje, R. Buckmaster, R. M. Overney, *Phys. Rev. Lett.* **2000**, 85, 2340.
- [3] O. Piétrement, M. Troyon, *Langmuir* **2001**, 17, 6540.
- [4] T. D. Li, H. C. Chiu, D. Ortiz-Young, E. Riedo, *Rev. Sci. Instrum.* **2014**, 85, 123707.

- [5] O. Piétrement, M. Troyon, *Surf. Interface Anal.* **2001**, 31, 1060.
- [6] L. Aldon, P. Kubiak, M. Womes, J. C. Jumas, J. Olivier-Fourcade, J. L. Tirado, J. I. Corredor, C. Pérez Vicente, *Chem. Mater.* **2004**, 16, 5721.
- [7] J. Serrano, A.H. Romero, F.J. Manjón, R. Lauck, M. Cardona, A. Rubio, *Phys. Rev. B* **2004**, 69, 094306.
- [8] S. Kalyanaraman, R.Thangavel, R.Vettumperumal, *J. Phys. Chem. Solids* **2013**, 74, 504.
- [9] H. Liu, Z. Zhu, J. Huang, X. He, Y. Chen, R. Zhang, R. Lin, Y. Li, S. Yu, X. Xing, Q. Yan, X. Li, M.J. Frost, K. An, J. Feng, R. Kostecki, H. Xin, S.P. Ong, P. Liu, *ACS Materials Letters* **2019**, 1, 96.
- [10] H. Ge, N. Li, D. Li, C. Dai, D. Wang, *The Journal of Physical Chemistry C.* **2009**, 113, 6324.
- [11] J. Chen, L. Yang, S. Fang, S.-i. Hirano, K. Tachibana, *Journal of Power Sources* **2012**, 200, 59.
- [12] F. Huang, J. Ma, H. Xia, Y. Huang, L. Zhao, S. Su, F. Kang, Y. B. He, *ACS Appl. Mater. Interfaces* **2019**, 11, 37357.
- [13] Chen Q, Yang Y, Zheng H, et al. Electrochemically Induced High Ion Conductive Porous Scaffold to Stabilize Lithium Deposition for Lithium Metal Anodes[J]. *Journal of Materials Chemistry A*, 2019.
- Q. Chen, Y. Yang, H. Zheng, Q. Xie, X. Yan, Y. Ma, L. Wang, D. L. Peng, *J. Mater. Chem. A* **2019**, 7, 11683.
- [14] Q. Chen, H. Li, M. L. Meyerson, R. Rodriguez, K. Kawashima, J. A. Weeks, H. Sun, Q. Xie, J. Lin, G. Henkelman, A. Heller, D.-L. Peng, C. B. Mullins, *ACS Appl. Mater. Interfaces* **2021**, 13, 9985.